

The CO-to-H₂ Conversion Factor across the Perseus Molecular Cloud

Min-Young Lee¹, Snežana Stanimirović¹, Mark G. Wolfire², Rahul Shetty³, Simon C. O. Glover³,
Faviola Z. Molina³, Ralf S. Klessen³

ABSTRACT

We derive the CO-to-H₂ conversion factor, $X_{\text{CO}} = N(\text{H}_2)/I_{\text{CO}}$, across the Perseus molecular cloud on sub-parsec scales by combining the dust-based $N(\text{H}_2)$ data with the I_{CO} data from the COMPLETE Survey. We estimate an average $X_{\text{CO}} \sim 3 \times 10^{19} \text{ cm}^{-2} \text{ K}^{-1} \text{ km}^{-1} \text{ s}$ and find a factor of ~ 3 variations in X_{CO} between the five sub-regions in Perseus. Within the individual regions, X_{CO} varies by a factor of ~ 100 , suggesting that X_{CO} strongly depends on local conditions in the interstellar medium. We find that X_{CO} sharply decreases at $A_V \lesssim 3$ mag but gradually increases at $A_V \gtrsim 3$ mag, with the transition occurring at A_V where I_{CO} becomes optically thick. We compare the $N(\text{HI})$, $N(\text{H}_2)$, I_{CO} , and X_{CO} distributions with two models of the formation of molecular gas, a one-dimensional photodissociation region (PDR) model and a three-dimensional magnetohydrodynamic (MHD) model tracking both the dynamical and chemical evolution of gas. The PDR model based on the steady state and equilibrium chemistry reproduces our data very well but requires a diffuse halo to match the observed $N(\text{HI})$ and I_{CO} distributions. The MHD model matches our data reasonably well, suggesting that time-dependent effects on H₂ and CO formation are insignificant for an evolved molecular cloud like Perseus. However, we find interesting discrepancies, including a broader range of $N(\text{HI})$, likely underestimated I_{CO} , and a large scatter of I_{CO} at small A_V . These discrepancies most likely result from strong compressions/rarefactions and density fluctuations in the MHD model.

1. Introduction

Stars form exclusively in molecular clouds, although the question whether molecular gas is a prerequisite or a byproduct of star formation is currently under debate (e.g., Glover & Clark 2012; Kennicutt & Evans 2012; Krumholz 2012). In either case, accurate measurements of the physical properties of molecular clouds are critical to constrain the initial conditions for star and molecular gas formation. However, obtaining such measurements is hampered by the fact that molecular hydrogen (H₂), the most abundant molecular species in the interstellar medium (ISM), is not directly observed under the typical conditions in molecular clouds. As a homonuclear diatomic molecule, H₂ does not have a permanent electric dipole moment and its ro-vibrational states change only via weak quadrupole transitions. Therefore, alternative tracers have been employed to infer the abundance and distribution of H₂.

Carbon monoxide (CO) is one of the most commonly used tracers of H₂ due to its large abundance and low rotational transitions that are readily excited in molecular clouds through collisions with H₂. In

¹Department of Astronomy, University of Wisconsin, Madison, WI 53706, USA; lee@astro.wisc.edu

²Department of Astronomy, University of Maryland, College Park, MD 20742, USA

³Zentrum für Astronomie der Universität Heidelberg, Institut für Theoretische Astrophysik, Albert-Ueberle-Str. 2, 69120 Heidelberg, Germany

particular, the $^{12}\text{CO}(J = 1 \rightarrow 0)$ integrated intensity⁴, I_{CO} , is often used to estimate the H_2 column density, $N(\text{H}_2)$, via the so-called “ X -factor”⁵, which is defined by

$$X_{\text{CO}} = \frac{N(\text{H}_2)}{I_{\text{CO}}} \quad \text{cm}^{-2} \text{ K}^{-1} \text{ km}^{-1} \text{ s}. \quad (1)$$

Accurate knowledge of X_{CO} is crucial to address some of the fundamental questions in astrophysics. For example, one of the most intriguing properties of galaxies is a strong power-law relation between the surface density of star formation rate, Σ_{SFR} , and the surface density of H_2 , Σ_{H_2} , generally known as the “Kennicutt-Schmidt relation” (e.g., Schmidt 1959; Kennicutt 1989; Bigiel et al. 2008; Schrubba et al. 2011; Rahman et al. 2012; Shetty et al. 2013). While this empirical relation provides important insights into the physical process of star formation (e.g., a close connection between the chemical or thermal state of the ISM and star formation), its precise form has been a subject of debate and strongly depends on X_{CO} .

From an observational perspective, X_{CO} is usually adopted as a conversion factor. Its estimate relies on the derivation of $N(\text{H}_2)$ using observational methods independent of CO (Bolatto et al. 2013 for a review). One of the methods to derive $N(\text{H}_2)$ utilizes dust as a tracer of total gas column density. Dust has been observed to be well mixed with gas (e.g., Boulanger et al. 1996) and can be mapped through its emission at far-infrared (FIR) wavelengths or its absorption at near-infrared (NIR) wavelengths. The procedure is to estimate the dust column density or the V -band extinction, A_V , from the FIR emission or the NIR absorption (e.g., Cardelli et al. 1989) and to assume or to estimate a dust-to-gas ratio (DGR) that linearly relates A_V to the total gas column density $N(\text{H}) = N(\text{HI}) + 2N(\text{H}_2)$. The atomic gas column density, $N(\text{HI})$, is then measured from the 21-cm emission and is removed from $N(\text{H})$ for an estimate of $N(\text{H}_2)$ (e.g., Israel 1997; Dame et al. 2001; Leroy et al. 2007, 2011; Lee et al. 2012; Sandstrom et al. 2013). The derived $N(\text{H}_2)$ is finally combined with I_{CO} to estimate X_{CO} .

This procedure has been applied to the Milky Way and a number of nearby galaxies. For the Milky Way, Dame et al. (2001) showed that X_{CO} does not change significantly with Galactic latitude (for $|b| \sim 5^\circ\text{--}30^\circ$) from the mean value of $(1.8 \pm 0.3) \times 10^{20}$ when molecular clouds are averaged over $\sim\text{kpc}$ scales. Several studies of individual molecular clouds at $3'\text{--}9'$ angular resolution have estimated similar average X_{CO} values (e.g., Frerking et al. 1982 for Ophiuchus; Lombardi et al. 2006 for Pipe; Pineda et al. 2008 for Perseus; Pineda et al. 2010 for Taurus; Paradis et al. 2012 for Aquila-Ophiuchus, Cepheus-Polaris, Taurus, and Orion). At the same time, X_{CO} values different from the Galactic mean value have been occasionally found, e.g., $X_{\text{CO}} \sim 0.5 \times 10^{20}$ for infrared cirrus clouds in Ursa Major (de Vries et al. 1987) and $X_{\text{CO}} \sim 6.1 \times 10^{20}$ for high-latitude clouds (Magnani et al. 1988), suggesting cloud-to-cloud variations in X_{CO} . Rare studies of X_{CO} in spatially resolved molecular clouds have shown some variations as well, e.g., $X_{\text{CO}} \sim (1.6\text{--}12) \times 10^{20}$ for Taurus (Pineda et al. 2010) and $X_{\text{CO}} \sim (0.9\text{--}1.8) \times 10^{20}$ for Perseus (Pineda et al. 2008). In studies of nearby galaxies on $\sim\text{kpc}$ scales, X_{CO} values are similar with the Galactic mean value and are relatively constant within individual galaxies. However, systematically smaller and larger X_{CO} values have been found from the central regions of star-forming galaxies (down to $\sim 0.1 \times 10^{20}$; e.g., Smith et al. 1991; Sandstrom et al. 2013) and low-metallicity dwarf irregular galaxies (up to $\sim 130 \times 10^{20}$; e.g., Israel 1997; Leroy et al. 2007; Gratier et al. 2010; Leroy et al. 2011), indicating the dependence of the average X_{CO} on interstellar environments.

From a theoretical perspective, X_{CO} has been primarily studied using photodissociation region (PDR)

⁴Hereafter $^{12}\text{CO}(J = 1 \rightarrow 0)$ is quoted as CO.

⁵Hereafter X_{CO} is quoted without its units.

models because the majority of the CO emission originates from the outskirts of molecular clouds, where the interstellar radiation field (ISRF) illuminates the cloud (e.g., Taylor et al. 1993; Le Bourlot et al. 1993; Wolfire et al. 1993; Kaufman et al. 1999; Bell et al. 2006; Wolfire et al. 2010). For example, Bell et al. (2006) used the UCL_PDR code (Papadopoulos et al. 2002) to calculate chemical abundances and emission strengths and showed that X_{CO} changes by more than an order of magnitude with varying depths within molecular clouds. In addition, they found significant variations in X_{CO} between molecular clouds with a wide range of physical parameters, e.g., density, metallicity, and cloud age. While the PDR models are limited to simple geometries and density distributions, three-dimensional magnetohydrodynamic (MHD) simulations have been recently performed to investigate X_{CO} in turbulent molecular clouds (e.g., Glover & Mac Low 2011; Shetty et al. 2011a,b). These simulations model chemistry for simple molecules such as H_2 and CO as a function of time and show that X_{CO} is not constant within individual clouds. Moreover, X_{CO} in simulations varies over four orders of magnitude between clouds with low densities, low metallicities, and strong radiation fields. Such variability of X_{CO} within resolved clouds and between clouds with different properties predicted by the PDR and MHD models has been rarely found in observations, largely due to the lack of high-resolution observations.

In this paper, we derive X_{CO} for the Perseus molecular cloud on sub-pc scales and test two theoretical models of the formation of molecular gas, in an attempt to understand the origins of the variations in X_{CO} and the physical processes of H_2 and CO formation. One model is the one-dimensional PDR model originally developed by Tielens & Hollenbach (1985) and updated by Kaufman et al. (2006), Wolfire et al. (2010), and Hollenbach et al. (2012). Here we use a further modification of this model, which allows for a two-sided illumination and either a constant density or a simple formulation of the density distribution (hereafter the modified W10 model). The other model is the three-dimensional MHD model by Shetty et al. (2011a) that is based on the modified ZEUS-MP code described in Glover et al. (2010) (hereafter the S11 model). There are two primary differences between these two models. First, the S11 model simulates H_2 and CO formation in turbulent molecular clouds by coupling the chemical and dynamical evolution of gas, while the modified W10 model takes into account the impact of turbulence only via a constant supersonic linewidth for spectral line formation and cooling. Second, the S11 model follows the time-dependent evolution of a number of chemical species, including H_2 and CO, while the modified W10 model uses a detailed time-independent chemical network that explicitly assumes chemical equilibrium for every atomic and molecular species. Therefore, we consider the modified W10 model and the S11 model as representative “microturbulent time-independent model” and “macroturbulent time-dependent model”. Our study is one of the first attempts to test the MHD model tracking both the chemical and dynamical evolution of the ISM and compare it with a more traditional view of the formation of molecular gas (PDR model). In addition, considering that small-scale ISM models are starting to be implemented in large-scale simulations of galaxy formation and evolution (e.g., Feldmann et al. 2012a,b; Lagos et al. 2012; Narayanan et al. 2012), our study will serve as a “zero point test” for the models of gas contents in galaxies.

We focus on the Perseus molecular cloud because of its proximity and a wealth of multi-wavelength observations. Located at a distance of $\sim 200\text{--}350$ pc (Herbig & Jones 1983; Černis 1990), Perseus has a projected angular size of $\sim 6^\circ \times 3^\circ$ on the sky. In this paper, we adopt the distance to Perseus of 300 pc. With a mass of $\sim 2 \times 10^4 M_\odot$ (Sancisi et al. 1974; Lada et al. 2010), Perseus is considered as a low-mass molecular cloud with an intermediate level of star formation (Bally et al. 2008). The cloud contains a number of dark (B5, B1E, B1, and L1448) and star-forming regions (IC348 and NGC1333) shown in Figure 1.

This paper is organized as follows. In Section 2, we summarize the results from previous studies highly

relevant to our investigation and provide constraints on important physical parameters of Perseus. In Section 3, we describe the multi-wavelength observations used in our study. In Section 4, we divide Perseus into a number of individual regions and select data points for each region. We then derive the X_{CO} image (Section 5) and investigate the large-scale spatial variations of X_{CO} and their correlations with physical parameters such as the strength of the radiation field and the CO velocity dispersion (Section 6). In addition, we examine how I_{CO} and X_{CO} change with A_V in Perseus. In Section 7, we summarize the details of the modified W10 model and the S11 model and compare our observational data with model predictions. Finally, we discuss and summarize our conclusions (Sections 8 and 9).

2. Background

2.1. Relevant Previous Studies of Perseus

Pineda et al. (2008) used the I_{CO} and A_V data from the COMPLETE Survey of Star Forming Regions (COMPLETE; Ridge et al. 2006) to investigate X_{CO} in Perseus. They fitted a linear function to I_{CO} vs A_V to estimate X_{CO} and found $X_{\text{CO}} \sim 1.4 \times 10^{20}$ for the whole cloud and a range of $X_{\text{CO}} \sim (0.9\text{--}1.8) \times 10^{20}$ for six sub-regions, suggesting a factor of ~ 2 spatial variations of X_{CO} caused by different ISM conditions. In the process of performing a linear fit, they noticed that X_{CO} is heavily affected by the saturation of I_{CO} at $A_V \gtrsim 4$ mag and re-estimated $X_{\text{CO}} \sim 0.7 \times 10^{20}$ from the linear fit only to the unsaturated I_{CO} . In addition, Pineda et al. (2008) compared the observed CO and $^{13}\text{CO}(J = 1 \rightarrow 0)$ integrated intensities with predictions from the Meudon PDR code (Le Petit et al. 2006) and found that the PDR models reproduce the CO and ^{13}CO observations reasonably well and the variations among the six sub-regions can be explained by variations in physical parameters, in particular density and non-thermal gas motion.

In our recent study, we derived the Σ_{HI} and Σ_{H_2} images of Perseus on ~ 0.4 pc scales (Section 3.1) and investigated how the H₂-to-HI ratio, $R_{\text{H}_2} = \Sigma_{\text{H}_2}/\Sigma_{\text{HI}} = 2N(\text{H}_2)/N(\text{HI})$, changes across the cloud (Lee et al. 2012). We found that Σ_{HI} is relatively uniform with $\sim 6\text{--}8 M_{\odot} \text{ pc}^{-2}$, while Σ_{H_2} significantly varies from $\sim 0 M_{\odot} \text{ pc}^{-2}$ to $\sim 73 M_{\odot} \text{ pc}^{-2}$, resulting in $R_{\text{H}_2} \sim 0\text{--}10$ with a mean of ~ 0.7 . Due to the nearly constant Σ_{HI} , a strong linear relation between R_{H_2} and $\Sigma_{\text{HI}} + \Sigma_{\text{H}_2}$ was found. Interestingly, these results are consistent with the time-independent H₂ formation model by Krumholz et al. (2009; hereafter the K09 model). In the K09 model, a spherical cloud is embedded in a uniform and isotropic radiation field and the H₂ abundance is estimated based on the balance between H₂ formation on dust grains and H₂ photodissociation by Lyman-Werner (LW) photons. The most important prediction of the K09 model is the minimum Σ_{HI} required to shield H₂ against photodissociation. This minimum Σ_{HI} for H₂ formation depends on metallicity (e.g., $\Sigma_{\text{HI}} \sim 10 M_{\odot} \text{ pc}^{-2}$ for solar metallicity) but only weakly on the strength of the radiation field. Once the minimum Σ_{HI} is achieved, additional Σ_{HI} is fully converted into Σ_{H_2} , resulting in the uniform Σ_{HI} distribution and the linear increase of R_{H_2} with $\Sigma_{\text{HI}} + \Sigma_{\text{H}_2}$.

2.2. Constraints on Physical Parameters

We summarize estimates of several important physical parameters of Perseus obtained from previous studies. We will use these parameters in later sections of this paper.

Density $n \sim 10^{3-4} \text{ cm}^{-3}$: Young et al. (1982) estimated $n \sim (1.7\text{--}5) \times 10^3 \text{ cm}^{-3}$ for B5 based on the large velocity gradient (LVG) model applied to CO and CO($J = 2 \rightarrow 1$) observations. Bensch (2006)

derived larger $n \sim (3-30) \times 10^3 \text{ cm}^{-3}$ for the same cloud by comparing PDR models with CO, ^{13}CO , and [CI] observations. Similarly, Pineda et al. (2008) found that PDR models with $n \sim \text{a few} \times 10^{3-4} \text{ cm}^{-3}$ can reproduce the CO and $^{13}\text{CO}(J = 1 \rightarrow 0)$ observations of Perseus. In summary, gas traced by the CO emission in Perseus is likely to have $n \sim 10^{3-4} \text{ cm}^{-3}$.

ISRF $G \sim 0.4 G'_0$: Lee et al. (2012) investigated the dust temperature, T_{dust} , across Perseus and potential heating sources and concluded that the cloud is embedded in the uniform Galactic ISRF heating dust grains to $\sim 17 \text{ K}$, except for the central parts of IC348 and NGC1333, where the radiation from internal B-type stars likely dominates. Under the assumption that dust grains are in thermal equilibrium, we can use $T_{\text{dust}} \sim 17 \text{ K}$ to estimate the strength of the radiation field by

$$G = 4.6 \times 10^{-11} \left(\frac{a}{0.1 \mu\text{m}} \right) T_{\text{dust}}^6 \text{ erg cm}^{-2} \text{ s}^{-1}, \quad (2)$$

where G is the flux at ultraviolet (UV) wavelengths and a is the size of dust grains (Lequeux 2005). Equation (2) assumes the absorption efficiency $Q_a = 1$ and the dust emissivity index $\beta = 2$. For dust grains with $a \sim 0.1 \mu\text{m}$, whose size is comparable to UV wavelengths therefore $Q_a \simeq 1$, we estimate $G \sim 1.1 \times 10^{-3} \text{ erg cm}^{-2} \text{ s}^{-1} \sim 0.4 G'_0$ (G'_0 = the local field measured in the solar neighborhood by Draine 1978 $\sim 2.7 \times 10^{-3} \text{ erg cm}^{-2} \text{ s}^{-1}$) for the uniform ISRF incident upon Perseus. The exceptions are the central regions of IC348 and NGC1333, where the radiation from the B-type stars is dominant.

Cosmic-ray ionization rate $\zeta \gtrsim 10^{-17} \text{ s}^{-1}$: There is emerging evidence that ζ likely lies between $\sim 10^{-17} \text{ s}^{-1}$ to $\sim 10^{-15} \text{ s}^{-1}$ with lower values in dense molecular clouds and $\sim 10^{-16} \text{ s}^{-1}$ to $\sim 10^{-15} \text{ s}^{-1}$ in the diffuse ISM (e.g., Dalgarno 2006; Indriolo & McCall 2012; Hollenbach et al. 2012). This suggests that ζ could be larger than the canonical $\zeta \sim 10^{-17} \text{ s}^{-1}$ by a factor of $\sim 10-100$ in the regions where the CO emission arises.

Metallicity $Z \sim 1 Z_{\odot}$: González Hernández et al. (2009) performed a chemical abundance analysis for Černis 52, a member of IC348 whose spectral type is A3 V, and derived $[\text{Fe}/\text{H}] = -0.01 \pm 0.15$ (corresponding to $Z \sim 0.7-1.4 Z_{\odot}$). In addition, Lee et al. (2012) compared the intensity at $100 \mu\text{m}$, I_{100} , with $N(\text{HI})$ for Perseus and found an overall linear relation. As $I_{100}/N(\text{HI})$ is an approximation of DGR, the fact that a single $I_{100}/N(\text{HI})$ fits most of the diffuse regions suggests no significant variation of DGR or Z across the cloud. Therefore, $Z \sim 1 Z_{\odot}$ would be a reasonable estimate for Perseus. Note that Lee et al. (2012) derived $\text{DGR} = A_V/N(\text{H}) \sim 1.1 \times 10^{-21} \text{ mag cm}^2$ for Perseus, which is ~ 2 times larger than the typical Galactic $\text{DGR} \sim 5.3 \times 10^{-22} \text{ mag cm}^2$ (Bohlin et al. 1978).

Turbulent linewidth $v_{\text{turb}} \lesssim 2-5 \text{ km s}^{-1}$: Pineda et al. (2008) compared the CO excitation temperature, T_{ex} , with A_V and found that T_{ex} increases from $\sim 5 \text{ K}$ at $A_V \sim 2 \text{ mag}$ to $\sim 20 \text{ K}$ at $A_V \gtrsim 4 \text{ mag}$. If $n > n_{\text{crit}} \sim 10^3 \text{ cm}^{-3}$ where n_{crit} is the critical density for the CO emission, the case likely for the regions with $A_V \gtrsim 4 \text{ mag}$, we expect that the CO emission is in local thermodynamic equilibrium (LTE) and $T_{\text{ex}} \sim T_{\text{k}}$ where T_{k} is the kinetic temperature. When we assume $T_{\text{ex}} \sim T_{\text{k}} \sim 20 \text{ K}$ for Perseus, the mean thermal velocity of CO-emitting gas would be $\langle v_{\text{th}} \rangle = \sqrt{2k_{\text{B}}T_{\text{k}}/\mu m_{\text{H}}} \sim 0.1 \text{ km s}^{-1}$ (k_{B} = the Boltzmann constant, μ = the mass of a molecule in amu = 28 for CO, m_{H} = the mass of a hydrogen atom). This $\langle v_{\text{th}} \rangle \sim 0.1 \text{ km s}^{-1}$ is an order of magnitude smaller than the CO velocity dispersion $\sigma_{\text{CO}} \sim 0.9-2 \text{ km s}^{-1}$ (corresponding to $\text{FWHM} = (8\ln 2)^{1/2} \sigma_{\text{CO}} \sim 2.1-4.7 \text{ km s}^{-1}$) measured across Perseus (Pineda et al. 2008). This suggests that there are most likely contributions from other processes, e.g., interstellar turbulence, systematic motions such as inflow, outflow, rotation, etc., and/or multiple components along a line of sight. For example, B1 and NGC1333 contain a large number of Herbig-Haro objects that are known to trace currently active shocks in outflows (e.g., Bally et al. 2008). Therefore, not all the observed σ_{CO}

should be attributed to interstellar turbulence alone. As a result, we expect v_{turb} to be smaller than the measured FWHM of $\sim 2\text{--}5 \text{ km s}^{-1}$.

Cloud age $t_{\text{age}} \sim 10 \text{ Myr}$: For IC348, Muench et al. (2003) derived a mean age of $\sim 2 \text{ Myr}$ with a spread of $\sim 3 \text{ Myr}$ using published spectroscopic observations. However, there are some indications for the existence of older stars in IC348. For example, Herbig (1998) found that $\text{H}\alpha$ emission line stars in IC348 have an age spread from $\sim 0.7 \text{ Myr}$ to $\sim 12 \text{ Myr}$. A similar spread in stellar age, from $\sim 0.5 \text{ Myr}$ to $\sim 10 \text{ Myr}$, has been found by Luhman et al. (1998) from their infrared and optical spectroscopic observations. Considering this duration of star formation in IC348, $t_{\text{age}} \sim 10 \text{ Myr}$ would be a reasonable age estimate for Perseus.

3. Data

3.1. Derived H_2 Distribution

We use the $N(\text{H}_2)$ image derived in our recent study, Lee et al. (2012). We used the $60 \mu\text{m}$ and $100 \mu\text{m}$ data from the Improved Reprocessing of the *IRAS* Survey (IRIS; Miville-Deschênes & Lagache 2005) to derive the dust optical depth at $100 \mu\text{m}$, τ_{100} . Dust grains were assumed to be in thermal equilibrium and the contribution from very small grains (VSGs) to the intensity at $60 \mu\text{m}$ was accounted for by calibrating the derived T_{dust} image with the T_{dust} data from Schlegel et al. (1998). The τ_{100} image was then converted into the A_V image by finding the conversion factor X for $A_V = X\tau_{100}$ that results in the best agreement between the derived A_V and COMPLETE A_V . This calibration of τ_{100} to COMPLETE A_V was motivated by Goodman et al. (2009), who found that dust extinction at NIR wavelengths is the best probe of total gas column density. Finally, Lee et al. (2012) estimated a local DGR for Perseus and derived the $N(\text{H}_2)$ image in combination with the HI data from the Galactic Arecibo L-band Feed Array HI Survey (GALFA-HI; Peek et al. 2011). The HI emission was integrated from -5 km s^{-1} to $+15 \text{ km s}^{-1}$, the range that maximizes the spatial correlation between the HI integrated intensity and the dust column density, and $N(\text{HI})$ was calculated under the assumption of optically thin HI. The derived $N(\text{H}_2)$ has a mean of $\sim 1.3 \times 10^{20} \text{ cm}^{-2}$ and peaks at $\sim 4.5 \times 10^{21} \text{ cm}^{-2}$. Its mean 1σ uncertainty is $\sim 3.6 \times 10^{19} \text{ cm}^{-2}$. See Section 4 of Lee et al. (2012) for details on the derivation of the $N(\text{H}_2)$ image and its 1σ uncertainty.

The T_{dust} , A_V , $N(\text{HI})$, and $N(\text{H}_2)$ images derived by Lee et al. (2012) are all at $4.3'$ angular resolution, corresponding to $\sim 0.4 \text{ pc}$ at the distance of 300 pc . We present the $N(\text{H}_2)$ image at $4.3'$ angular resolution in Figure 2. The blank data points correspond to point sources and regions with possible contamination (the Taurus molecular cloud and a background HII region). See Sections 4.2 and 4.3 of Lee et al. (2012) for details.

3.2. Observed CO Distribution

We use the COMPLETE CO data cube obtained with the 14-m FCRAO telescope (Ridge et al. 2006). This cube covers the main body of Perseus with a spatial area of $\sim 6^\circ \times 3^\circ$ at $46''$ angular resolution. We correct the CO data for the main-beam efficiency of 0.45, following Ridge et al. (2006) and Pineda et al.

(2008). The rms noise per channel⁶ ranges from ~ 0.3 K to ~ 3.5 K with a mean of ~ 0.8 K. We show the average CO spectrum for Perseus in Figure 3. To produce this spectrum, we average the spectra of all data points where the ratio of the peak main-beam brightness temperature to the rms noise is greater than 3. The CO emission is clearly contained between -5 km s⁻¹ and $+15$ km s⁻¹ and shows multiple velocity components.

To derive I_{CO} , we integrate the CO emission from -5 km s⁻¹ to $+15$ km s⁻¹, the range where Lee et al. (2012) found the HI emission associated with Perseus, with a spectral resolution of 0.064 km s⁻¹. At $46''$ angular resolution, the derived I_{CO} ranges from -19.9 K km s⁻¹ to 116.6 K km s⁻¹. Its mean 1σ uncertainty is ~ 0.9 K km s⁻¹. We note that some data points in the CO cube are affected by an artificial absorption feature at $v \sim 7.5$ km s⁻¹. This artifact is due to the contaminated off-position⁷ and is responsible for a number of blanked data points in Figure 6 that do not correspond to point sources and regions with possible contamination. We find that this artifact does not affect our estimate of I_{CO} .

4. Region Division

As pointed out by Pineda et al. (2008) and Lee et al. (2012), there are considerable region-to-region variations in physical parameters across Perseus. We therefore divide the cloud into five regions and perform analyses mainly on the individual regions. To define the individual regions, we draw the COMPLETE I_{CO} contours from 4 K km s⁻¹ (5% of the peak) to 72 K km s⁻¹ (90% of the peak) with 4 K km s⁻¹ intervals and use the contours to determine the boundaries of each region. Note that the minimum I_{CO} of 4 K km s⁻¹ for the regional boundaries does not mean that there is no data point with $I_{\text{CO}} < 4$ K km s⁻¹. In addition, we select data points that have (1) -5 km s⁻¹ < CO velocity centroid < $+15$ km s⁻¹, (2) $I_{\text{CO}} > 0$ K km s⁻¹, and (3) $N(\text{H}_2) > 0$ cm⁻². These criteria are to select data points that are reliable and kinematically associated with Perseus. Applying these criteria results in 1160 independent data points and all except three data points have $S/N > 1$ for both I_{CO} and $N(\text{H}_2)$. We show the selected data points for each region (B5, B1E/B1, L1448 as dark regions and IC348, NGC1333 as star-forming regions) with a different color in Figure 4. The individual regions have an average size of ~ 5 – 7 pc at the distance of 300 pc (Table 1).

5. Deriving X_{CO}

We derive the X_{CO} image at $4.3'$ angular resolution by applying Equation (1) to the $N(\text{H}_2)$ image and the COMPLETE I_{CO} image (smoothed to match the angular resolution of the $N(\text{H}_2)$ image) on a pixel-by-pixel basis (Figure 5). For the five regions defined in Section 4, X_{CO} ranges from $\sim 5.7 \times 10^{15}$ to $\sim 4.4 \times 10^{21}$. While X_{CO} shows a substantial range, most data points ($\sim 80\%$) have $10^{19} < X_{\text{CO}} < 10^{20}$. Summing both $N(\text{H}_2)$ and I_{CO} over all five regions results in an average $\langle X_{\text{CO}} \rangle = \Sigma N(\text{H}_2) / \Sigma I_{\text{CO}} \sim 3 \times 10^{19}$. Applying a single criterion of $N(\text{H}_2) > 0$ cm⁻² to the whole cloud to include the regions with H₂ but without CO detection results in the same average $\langle X_{\text{CO}} \rangle \sim 3 \times 10^{19}$. The 1σ uncertainty of X_{CO} is derived based on the propagation of errors (Bevington & Robinson 2003) and its mean value is $\sim 1.6 \times 10^{19}$.

⁶In this paper, all temperatures are in main-beam brightness units and all velocities are quoted in the local standard of rest (LSR) frame.

⁷See http://www.cfa.harvard.edu/COMPLETE/data_html_pages/PerA_12coFCRAO_F.html.

6. Results

6.1. Large-scale Spatial Variations of X_{CO}

Figure 5 shows interesting spatial variations of X_{CO} across Perseus. To quantify these variations, we estimate the $\langle X_{\text{CO}} \rangle$ values for the dark and star-forming regions by summing $N(\text{H}_2)$ and I_{CO} over each region (Table 1). We find a factor of ~ 3 decrease in X_{CO} from the northeastern regions (B5 and IC348) where $\langle X_{\text{CO}} \rangle \sim 6 \times 10^{19}$ to the southwestern regions (B1E/B1, NGC1333, and L1448) where $\langle X_{\text{CO}} \rangle \sim 2 \times 10^{19}$. Our result is consistent with Pineda et al. (2008) in that both studies found regional variations of X_{CO} across Perseus. However, while they estimated a single X_{CO} for each sub-region, we derived the spatial distribution of X_{CO} . Based on this distribution, we investigate large-scale trends in several physical parameters and their possible connections with the variations of X_{CO} .

We first derive the σ_{CO} image using the COMPLETE CO data cube. Figure 6 shows that the southwestern part has systematically larger σ_{CO} than the northeastern part. For example, $\sim 70\%$ of the data points in the southwestern part have $\sigma_{\text{CO}} > 1.5 \text{ km s}^{-1}$, while $\sim 40\%$ of the data points in the northeastern part have $\sigma_{\text{CO}} > 1.5 \text{ km s}^{-1}$. In particular, B1E/B1 and NGC1333 have the largest median $\sigma_{\text{CO}} \sim 2 \text{ km s}^{-1}$ compared to other regions where the median σ_{CO} is $\sim 1.3 \text{ km s}^{-1}$ (Table 1). The large σ_{CO} in the southwestern part could be caused by more complex velocity structure and/or multiple components along a line of sight. In addition, outflows from embedded protostars could contribute to broaden the CO spectra. For example, B1 and NGC1333 have many Herbig-Haro objects identified from the surveys of $\text{H}\alpha$ and [SII] emission, which trace currently active shocks in outflows (e.g., Bally et al. 2008).

The T_{dust} image derived by Lee et al. (2012) also shows systematic variations across Perseus. Specifically, T_{dust} slightly decreases toward the southwestern part. This is consistent with Pineda et al. (2008), who found $T_{\text{dust}} \sim 17 \text{ K}$ for B5/IC348 and $T_{\text{dust}} \sim 16 \text{ K}$ for B1E/B1/NGC1333. To investigate the variations of ISRF, We evaluate G using Equation (2) and assess its distributions for B5/IC348 (*East*) and B1E/B1/NGC1333/L1448 (*West*). Figure 7 shows the median G of *East* ($\sim 10^{-2.86} \text{ erg cm}^{-2} \text{ s}^{-1}$) as a dashed line. We find that $\sim 50\%$ and $\sim 2\%$ of the data points have $G > 10^{-2.86} \text{ erg cm}^{-2} \text{ s}^{-1}$ for *East* and *West* respectively. This suggests that G systematically decreases toward the southwestern part of Perseus. However, the variation of G is very mild: the median G decreases from *East* to *West* by only a factor of ~ 1.4 . This result does not change even when we examine the median G for each dark and star-forming region.

Finally, Lee et al. (2012) noticed a considerable difference between the northeastern and southwestern parts of Perseus regarding the relative spatial distribution of H_2 and CO. They estimated the fraction of “CO-dark” H_2 , which refers to interstellar gas in the form of H_2 along with CI and CII but little or no CO, and found a factor of ~ 3 decrease in the fraction toward the southwestern part. In other words, “CO-free” H_2 envelopes exist in the northeastern part, while CO traces H_2 reasonably well in the southwestern part (e.g., Figure 14 of Lee et al. 2012). This suggests that H_2 takes up a larger volume than CO in the northeastern region, which could result in larger X_{CO} .

Many theoretical studies have shown that X_{CO} can vary over several orders of magnitude with changes in density, metallicity, turbulent linewidth, ISRF, etc. (e.g., Maloney & Black 1988; Le Bourlot et al. 1993; Wolfire et al. 1993; Sakamoto 1996, 1999; Kaufman et al. 1999; Bell et al. 2006; Glover & Mac Low 2011; Shetty et al. 2011a,b), suggesting that various physical parameters play a role in determining X_{CO} . This likely applies to Perseus as well. While σ_{CO} and G show some interesting variations across the cloud, their correlations with X_{CO} are not strong (Spearman’s rank correlation coefficient $r_s = -0.2$ and 0.6 respectively; the null hypothesis is rejected at the 99% two-tailed confidence level). In addition, as we will

show in comparison with the modified W10 model (Section 7.1), changes in density appear to contribute to the observed variations in X_{CO} as well. It is most likely, therefore, that combinations of changes in density, turbulent linewidth, ISRF, and possibly other parameters we do not test in our study result in the variations in X_{CO} across the cloud. This conclusion is consistent with Pineda et al. (2008), who suggested that local variations in density, non-thermal gas motion, and ISRF can explain the observed scatter of X_{CO} among the sub-regions in Perseus.

Because X_{CO} depends on many properties of the ISM, constraining physical conditions by matching models to the observed value of X_{CO} requires a search through a large parameter space. Nevertheless, from a theoretical standpoint, X_{CO} has an interesting characteristic dependence on A_V (e.g., Taylor et al. 1993, Bell et al. 2006; Glover & Mac Low 2011; Shetty et al. 2011a; Feldmann et al. 2012a). We focus on investigating this characteristic dependence over a broad range of A_V by comparing our observations with two different theoretical models, with an aim of understanding the important physical processes of H_2 and CO formation. To do so, we use the models with a simple set of input parameters reasonable for Perseus and focus mainly on the general trends of $N(\text{HI})$, $N(\text{H}_2)$, I_{CO} , and X_{CO} with A_V .

6.2. I_{CO} versus A_V

6.2.1. Global Properties

To understand how X_{CO} varies with A_V , we begin by plotting I_{CO} as a function of A_V in Figure 8 for all five regions defined in Section 4. We use the A_V image at $4.3'$ angular resolution derived by Lee et al. (2012). Even though there is a large amount of scatter, several important features are noticeable.

First, there appears to be some threshold $A_{V,\text{th}} \sim 1$ mag below which no CO emission is detected. The sharp increase of I_{CO} with A_V found from the individual regions (Section 6.2.2) strongly supports the existence of such threshold. This may suggest that CO becomes shielded against photodissociation at $A_V \sim 1$ mag in Perseus. Previous observations of molecular clouds have found the similar $A_{V,\text{th}} \sim 1$ mag (e.g., Lombardi et al. 2006; Pineda et al. 2008; Leroy et al. 2009). Note that a lack of CO detection at $A_V \lesssim 1$ mag is not due to our sensitivity, considering that our mean 1σ uncertainty of A_V is ~ 0.2 mag. In addition, the threshold is not the result of the limited spatial coverage of the COMPLETE I_{CO} image. We made a comparison between our A_V image and the I_{CO} image with a large spatial area of $\sim 10^\circ \times 7^\circ$ from the Center for Astrophysics CO Survey (CfA; Dame et al. 2001) at the common angular resolution of $8.4'$ and found essentially the same threshold.

Second, I_{CO} significantly increases from ~ 0.1 K km s $^{-1}$ to ~ 70 K km s $^{-1}$ for a narrow range of $A_V \sim 1$ –3 mag. This steep increase of I_{CO} may suggest that the transition from CII/CI to CO is sharp once shielding becomes sufficiently strong to prevent photodissociation (e.g., Taylor et al. 1993; Bell et al. 2006).

Third, I_{CO} gradually increases and saturates to ~ 50 –80 K km s $^{-1}$ at $A_{V,\text{sat}} \gtrsim 3$ mag. This is consistent with Pineda et al. (2008), who found $A_{V,\text{sat}} \sim 4$ mag for Perseus. Similarly, Lombardi et al. (2006) found the saturation of $I_{\text{CO}} \sim 30$ K km s $^{-1}$ for the Pipe nebula at $A_{V,\text{sat}} \sim 6$ mag (with their adopted relation $A_V = A_K/0.112$). The saturation of I_{CO} is expected based on the relation between I_{CO} and τ , $I_{\text{CO}} \propto 1 - e^{-\tau}$, where $\tau \propto A_V$. Therefore, I_{CO} does not faithfully trace A_V once it becomes optically thick. The presence of optically thick CO emission in Perseus was hinted by Pineda et al. (2008), who performed the curve of growth analysis for the CO and $^{13}\text{CO}(J = 1 \rightarrow 0)$ observations.

6.2.2. Individual Regions

In agreement with Pineda et al. (2008), we find that the relation between I_{CO} and A_V has significant region-to-region variations across Perseus, contributing to the large scatter in Figure 8. We therefore show I_{CO} vs A_V for each dark and star-forming region in Figure 9. To emphasize the steep increase and saturation of I_{CO} , we plot I_{CO} as a function of A_V on a log-log scale.

Among the five regions, B5 and L1448 have the narrowest range of $A_V \sim 1\text{--}3$ mag, simply reflecting their smaller $N(\text{H})$ range on average. On the other hand, IC348 has the largest ranges of $A_V \sim 1\text{--}11$ mag and $I_{\text{CO}} \sim 0.2\text{--}50$ K km s⁻¹. I_{CO} steeply increases from ~ 0.2 K km s⁻¹ to ~ 35 K km s⁻¹ at $A_V \sim 1\text{--}3$ mag and then saturates to ~ 50 K km s⁻¹ at $A_V \gtrsim 3$ mag. In the case of B1E/B1, two components are apparent. The first component corresponds to the relatively steep increase of I_{CO} from ~ 1 K km s⁻¹ to ~ 20 K km s⁻¹ at $A_V \sim 1.5\text{--}3$ mag. The second component corresponds to the gradual increase of I_{CO} from ~ 20 K km s⁻¹ to ~ 60 K km s⁻¹ at $A_V \sim 1.5\text{--}5$ mag. Considering the two components together, I_{CO} saturates to ~ 60 K km s⁻¹ at $A_V \gtrsim 3$ mag. Lastly, NGC1333 has the majority of the data points ($\sim 90\%$) at $A_V \lesssim 3$ mag. I_{CO} increases from ~ 0.5 K km s⁻¹ to ~ 70 K km s⁻¹ at $A_V \sim 1\text{--}3$ mag and then shows a hint of the saturation to ~ 80 K km s⁻¹ at $A_V \gtrsim 3$ mag. Note that NGC1333 is the region where I_{CO} saturates to the largest value in Perseus.

In summary, the most important properties we find from the individual regions are the abrupt increase of I_{CO} at $A_V \lesssim 3$ mag and the saturation of I_{CO} at $A_V \gtrsim 3$ mag. However, I_{CO} saturates to different values, from ~ 50 K km s⁻¹ for IC348 to ~ 80 K km s⁻¹ for NGC1333.

6.3. X_{CO} versus A_V

Our derived spatial distribution of X_{CO} allows us to test interesting theoretical predictions such as the dependence of X_{CO} on A_V . In Figure 10, we plot X_{CO} as a function of A_V for each dark and star-forming region. While B5 and L1448 do not show a clear relation between X_{CO} and A_V due to their narrow range of A_V , IC348 has a distinct trend of X_{CO} decreasing at small A_V and increasing at large A_V . X_{CO} decreases by a factor of ~ 70 at $A_V \sim 1\text{--}2.5$ mag and increases by only a factor of ~ 4 at $A_V \sim 2.5\text{--}11$ mag. In the case of B1E/B1, there appears to be two components. The majority of the data points show a linear increase of X_{CO} from $\sim 7 \times 10^{18}$ to $\sim 5 \times 10^{19}$ for $A_V \sim 1.5\text{--}5$ mag. The additional group of the data points is located at $A_V \sim 2\text{--}3$ mag and $X_{\text{CO}} \sim 10^{20}$ with some scatter. Finally, NGC1333 has the majority of the data points ($\sim 83\%$) at $A_V \lesssim 3$ mag and $X_{\text{CO}} \lesssim 5 \times 10^{19}$ with a large degree of scatter (a factor of ~ 10). At $A_V \sim 3\text{--}10$ mag, X_{CO} increases by only a factor of ~ 4 . Overall, we find a factor of up to ~ 100 variations in X_{CO} for IC348, B1E/B1, and NGC1333 with a size of $\sim 6\text{--}7$ pc.

We notice that the shape of the X_{CO} vs A_V profiles is primarily driven by how I_{CO} changes with A_V . Specifically, decreasing X_{CO} with A_V results from the steep increase of I_{CO} at small A_V , while increasing X_{CO} with A_V is due to the saturation of I_{CO} at large A_V . X_{CO} decreases because I_{CO} increases more steeply than $N(\text{H}_2)$ likely due to the sharp transition from CII/CI to CO. On the other hand, X_{CO} increases because I_{CO} increases gradually compared to $N(\text{H}_2)$ likely due to the saturation of I_{CO} resulted from the large optical depth. Therefore, the transition from decreasing to increasing X_{CO} occurs in the X_{CO} vs A_V profile where the CO emission becomes optically thick. This is particularly prominent for IC348, where this transition occurs at $A_V \sim 3$ mag. B1E/B1 is relatively similar with IC348, while we do not observe a clear indication of this transition for NGC1333. Several theoretical studies have predicted the similar shape for the X_{CO} vs A_V profile (e.g., Taylor et al. 1993; Bell et al. 2006; Glover & Mac Low 2011; Shetty et al.

2011a; Feldmann et al. 2012a). In the next sections, we compare our X_{CO} data with predictions from two models.

7. X_{CO} : Comparison between Observations and Theory

7.1. Microturbulent Time-independent Model

7.1.1. Summary of the Modified W10 Model

We use a modified form of the model in Wolfire et al. (2010) to calculate H_2 and CO abundances and CO line emission. The model in Wolfire et al. (2010) uses a plane-parallel PDR code with one-sided illumination to estimate the distributions of atomic and molecular species as a function of A_V into a cloud. The density distribution is taken to be the median density as expected from turbulence and the distribution is converted into a spherical geometry. In our modified W10 model, a plane-parallel slab of gas is illuminated by UV photons on two sides and has either a uniform density distribution or a distribution described with a simple step function. The gas temperature and the abundances of atomic and molecular species are calculated as a function of A_V under the assumptions of thermal balance and chemical equilibrium. For details on the chemical and thermal processes, we refer the reader to Tielens & Hollenbach (1985), Kaufman et al. (2006), Wolfire et al. (2010), and Hollenbach et al. (2012).

The input parameters for the modified W10 model are n , G , ζ , v_{turb} , Z , and DGR. Considering the constraints on the physical parameters of Perseus (Section 2.2), we use a set of the modified W10 models with the following inputs: $G = 0.5 G'_0$, $\zeta = 10^{-16} \text{ s}^{-1}$, $v_{\text{turb}} = 4 \text{ km s}^{-1}$, $Z = 1 Z_{\odot}$, and $\text{DGR} = 1 \times 10^{-21} \text{ mag cm}^2$. For the density distribution, we use both a uniform density distribution with $n = 10^3$, 5×10^3 , and 10^4 cm^{-3} and a “core-halo” density distribution. The “halo” consists of HI with a fixed density $n_{\text{halo}} = 40 \text{ cm}^{-3}$, comparable to diffuse cold neutral medium (CNM) clouds (Wolfire et al. 2003), and has $N(\text{HI}) = 4.5 \times 10^{20} \text{ cm}^{-2}$ on each side of the slab. In the “core”, on the other hand, n abruptly increases to a large density $n_{\text{core}} = 10^3$, 5×10^3 , or 10^4 cm^{-3} . This “core-halo” structure is motivated by observations of molecular clouds that have found HI envelopes with $N(\text{HI}) \sim 10^{21} \text{ cm}^{-2}$ (e.g., Imara & Blitz 2011; Imara, Bigiel, & Blitz 2011; Lee et al. 2012). As the minimum density of the densest regions for both the uniform and “core-halo” density distributions ($\sim 10^3 \text{ cm}^{-3}$) has already been constrained by previous comparisons between CO observations and LVG/PDR models (Section 2.2), we expect that the modified W10 model with density much smaller than 10^3 cm^{-3} would not reproduce the observed I_{CO} in Perseus and therefore do not demonstrate the effect of n , $n_{\text{core}} < 10^3 \text{ cm}^{-3}$ in this paper. In addition, we note that the modified W10 model is not sensitive to the exact value of n_{halo} , as long as this is small enough to contain a small amount of H_2 and CO in the halo (Section 7.1.2 for details).

We run the model for $A_V = 0.6, 0.8, 1, 1.5, 2, 2.8, 4.8, 7.2, 10 \text{ mag}$ (uniform density) and $A_V = 1.25, 1.3, 1.5, 1.7, 2, 2.8, 4.8, 7.2, 10 \text{ mag}$ (“core-halo”) and the output quantities are $N(\text{HI})$, $N(\text{H}_2)$, and I_{CO} for a given A_V . We summarize the ranges of the output quantities in Tables 2 (“core-halo”) and 3 (uniform density). Note that for both the uniform and “core-halo” density distributions an increase in A_V can be thought of as an increase in size of the dense region. For example, $A_V = \text{DGR} \times N(\text{H}) = \text{DGR}(n_{\text{core}}L_{\text{core}} + n_{\text{halo}}L_{\text{halo}}) = 3.1 \times 10^{-3} L_{\text{core}}n_{\text{core}} + 0.9 \text{ mag}$, with L_{core} in units of pc and n_{core} in units of cm^{-3} for the “core-halo” density distribution. The “core” has a typical size $L_{\text{core}} \lesssim 1 \text{ pc}$, while the “halo” is significantly more extended with $L_{\text{halo}} \sim 7 \text{ pc}$. For the uniform density distribution, the size of the slab is generally $L_{\text{uniform}} \lesssim 1 \text{ pc}$. We note that in the most extreme case the size of the dense region is much smaller than

our spatial resolution ($L_{\text{core}} \sim 0.01$ pc), implying a considerably small filling factor of the “core” relative to the “halo”, but comparable to the size of small-scale clumps observed in the CO emission (e.g., Heithausen et al. 1998; Kramer et al. 1998).

7.1.2. Comparison with Observations: “Core-halo” Density Distribution

We compare X_{CO} vs A_V with predictions from the modified W10 model (“core-halo”) in Figure 11(a). While B5 and L1448 probe too narrow ranges of A_V for significant comparisons, the model curves with $n_{\text{core}} = 10^{3-4} \text{ cm}^{-3}$ follow the observed trends for IC348 and B1E/B1. The situation is more complicated for NGC1333, where the model matches the observed X_{CO} only for a partial range of A_V and has difficulties in reproducing the observations at $A_V \lesssim 3$ mag and $X_{\text{CO}} \lesssim 10^{19}$. In addition, NGC1333 lacks the decreasing portion of the X_{CO} vs A_V profile because of the missing data points with small $I_{\text{CO}} \lesssim 10 \text{ K km s}^{-1}$. Here we provide a description of the detailed comparison between our data of IC348, B1E/B1, and NGC1333 and the modified W10 model.

- (1) For IC348, the model with $n_{\text{core}} = 10^3 \text{ cm}^{-3}$ reproduces well the observed shape of the X_{CO} vs A_V profile (decreasing X_{CO} at $A_V \lesssim 3$ mag and increasing X_{CO} at $A_V \gtrsim 3$ mag).
- (2) For B1E/B1, the model with n_{core} varying from 10^3 cm^{-3} to 10^4 cm^{-3} can reproduce the observed shape of the X_{CO} and A_V profile.
- (3) For NGC1333, the observed scatter at small A_V calls for a range of $n_{\text{core}} \sim 10^{3-4} \text{ cm}^{-3}$. Considering that the models with $n_{\text{core}} = 5 \times 10^3 \text{ cm}^{-3}$ and 10^4 cm^{-3} are essentially identical, however, the data points at $A_V \lesssim 3$ mag with $X_{\text{CO}} \lesssim 10^{19}$ would not be reproduced by the model with $n_{\text{core}} > 10^4 \text{ cm}^{-3}$. In addition, our observational data lack the decreasing portion of the X_{CO} vs A_V profile. We suspect that this is due to the limited spatial coverage of the COMPLETE I_{CO} image, which does not adequately sample low column density regions for NGC1333 (only $\sim 10\%$ of the data points have $I_{\text{CO}} < 10 \text{ K km s}^{-1}$).

In Figure 11(b), we compare the observed X_{CO} vs $N(\text{H}_2)$ profiles with the model and find similar results. In summary, the modified W10 model with the “core-halo” structure and the input parameters appropriate for Perseus predicts the ranges of I_{CO} and $N(\text{H}_2)$ in good agreement with our data. IC348 and B1E/B1 are the best cases where the shape of the X_{CO} vs A_V profiles and the location of the minimum X_{CO} are well described by the model. We note that there are some discrepancies at low column densities in NGC1333, where the data points with $X_{\text{CO}} \lesssim 10^{19}$ are not reproduced by the model and at the same time the observed data with $X_{\text{CO}} \gtrsim 10^{20}$ are missing due to the limited observational coverage.

Next, we plot $N(\text{HI})$ as a function of $N(\text{H})$ in Figure 11(c) and compare the profiles with the modified W10 model. As summarized in Section 2.1, Lee et al. (2012) found a relatively uniform $N(\text{HI})$ distribution across Perseus with $\sim (8-10) \times 10^{20} \text{ cm}^{-2}$. Here we use the same $N(\text{HI})$ image as in Lee et al. (2012) and apply the same boundaries for the five regions as in Section 4. We find that the mean $N(\text{HI})$ varies from $\sim 7.4 \times 10^{20} \text{ cm}^{-2}$ (B5) to $\sim 9.6 \times 10^{20} \text{ cm}^{-2}$ (NGC1333 and L1448). The model predicts $N(\text{HI}) \sim (9-9.6) \times 10^{20} \text{ cm}^{-2}$, with essentially no difference between $n_{\text{core}} = 10^3 \text{ cm}^{-3}$ and 10^4 cm^{-3} models. The predicted $N(\text{HI})$ distribution with $\sim 9 \times 10^{20} \text{ cm}^{-2}$ and its uniformity are consistent with what we observe in Perseus. This agreement will persist even if the $N(\text{HI})$ distribution is corrected for high optical depth HI. Our preliminary work on the effect of high optical depth HI that is missing in the HI emission image of Perseus shows that $N(\text{HI})$ increases by a factor of ~ 1.5 at most due to the optical depth correction (the corrected $N(\text{HI}) \sim (8-18) \times 10^{20} \text{ cm}^{-2}$; Stanimirović et al. in prep). The ranges of the predicted $N(\text{HI})$

and $N(\text{H}_2)$ distributions are comparable to what we find in Perseus. In Figure 11(d), we plot R_{H_2} against $N(\text{H})$ and indeed find that the model matches well our observations. In particular, the linearly increasing R_{H_2} with $N(\text{H})$ is reproduced well by the model, mainly driven by the uniform $N(\text{HI})$ distribution.

7.1.3. Comparison with Observations: Uniform Density Distribution

So far we made comparisons between the observations of Perseus and the modified W10 model with the “core-halo” structure. To investigate the role of the diffuse halo in determining H_2 and CO distributions, we show our data for IC348 and predictions from the modified W10 model both with the “core-halo” structure and the uniform density distribution in Figure 12. The uniform density distribution simply assumes a dense core with $n = 10^3$, 5×10^3 , or 10^4 cm^{-3} . Clearly, the “core-halo” model describes our data better. For example, the uniform density model underestimates the $N(\text{HI})$ distribution compared to the observed one across the cloud. In addition, it predicts the decreasing portion of the X_{CO} vs A_V profile shallower than our data, while reproducing the observed range of X_{CO} reasonably well. We compare the “core-halo” model with the uniform density model in detail as follows.

$N(\text{HI})$ vs $N(\text{H})$: The uniform density model predicts $N(\text{HI})$ significantly smaller than what we measure across Perseus, $N(\text{HI}) \sim 9 \times 10^{20} \text{ cm}^{-2}$. The discrepancy ranges from a factor of ~ 10 – 20 for $n = 10^3 \text{ cm}^{-3}$ to a factor of ~ 70 – 160 for $n = 10^4 \text{ cm}^{-3}$. This large discrepancy results from the fact that H_2 self-shielding is so strong that almost all hydrogen is converted into H_2 . On the other hand, the density of the halo is small enough that dust shielding is more important than H_2 self-shielding. To provide the sufficient dust shielding for H_2 formation, the entire halo remains atomic with its initial $N(\text{HI}) \sim 9 \times 10^{20} \text{ cm}^{-2}$, resulting in the uniform $N(\text{HI})$ distribution. We expect that if the density of the halo is significantly larger than the current $n_{\text{halo}} = 40 \text{ cm}^{-3}$, the halo will no longer be purely atomic due to the increased H_2 self-shielding.

$N(\text{H}_2)$ vs $N(\text{H})$: All models predict the $N(\text{H}_2)$ vs $N(\text{H})$ profile in good agreement with our data, even though the uniform density model slightly overestimates $N(\text{H}_2)$ at small $N(\text{H})$. For example, the uniform density model with $n = 10^4 \text{ cm}^{-3}$ predicts $N(\text{H}_2) = 9.96 \times 10^{20} \text{ cm}^{-2}$ at $N(\text{H}) = 2 \times 10^{21} \text{ cm}^{-2}$, larger than our data by less than a factor of 2. However, this discrepancy is significant at such small $N(\text{H})$ and results in the small amount of $N(\text{HI}) \lesssim 10^{19} \text{ cm}^{-2}$. In addition, models with different densities predict essentially the same $N(\text{H}_2)$ for a given $N(\text{H})$. All these results imply that neither density nor its distribution is critical for the H_2 abundance. Instead, $N(\text{H})$ primarily determines $N(\text{H}_2)$.

R_{H_2} vs $N(\text{H})$: While the “core-halo” model reproduces both the range of R_{H_2} and the linear increase of R_{H_2} with $N(\text{H})$, the uniform density model overestimates R_{H_2} for a given $N(\text{H})$ by up to a factor of ~ 300 . This discrepancy mainly results from the significantly underestimated $N(\text{HI})$ in the uniform density model.

I_{CO} vs $N(\text{H}_2)$: All models reproduce the observed I_{CO} vs $N(\text{H}_2)$ profile reasonably well. In particular, both the “core-halo” and uniform density models with the smallest density show an excellent agreement with our data for IC348. While the models with $n \gtrsim 5 \times 10^3 \text{ cm}^{-3}$ and $n_{\text{core}} \gtrsim 5 \times 10^3 \text{ cm}^{-3}$ predict larger I_{CO} at small $N(\text{H}_2)$ (up to a factor of ~ 10), the difference between the models with different densities becomes negligible at $N(\text{H}_2) \gtrsim 1 \times 10^{21} \text{ cm}^{-2}$, where I_{CO} saturates to ~ 45 – 60 K km s^{-1} for the uniform density model and ~ 30 – 40 K km s^{-1} for the “core-halo” model. All these results suggest that I_{CO} depends on density but only at small $N(\text{H}_2)$ and changes in physical parameters other than density (e.g., v_{turb}) will be required to produce larger I_{CO} values once I_{CO} becomes optically thick.

I_{CO} vs A_V : While the “core-halo” model reproduces the sharp increase of I_{CO} observed at $A_V \gtrsim 1 \text{ mag}$,

the uniform density model predicts the increase of I_{CO} at $A_V \gtrsim 0.6$ mag much more gradually than our data. This difference comes from the fact that the uniform density model has larger density than the “core-halo” model, resulting in the larger I_{CO} for a given $A_V \lesssim 3$ mag ($n \gtrsim 10^3 \text{ cm}^{-3}$ for the uniform density model vs $\langle n \rangle \sim 55\text{--}125 \text{ cm}^{-3}$ for the “core-halo” model; Table 2). On the other hand, all models predict the saturation of I_{CO} to similar values at $A_V \gtrsim 3$ mag, suggesting that the larger density in the uniform density model no longer has a significant impact on I_{CO} due to the large optical depth of I_{CO} ($n \gtrsim 10^3 \text{ cm}^{-3}$ for the uniform density model vs $\langle n \rangle \sim 180\text{--}430 \text{ cm}^{-3}$ for the “core-halo” model; Table 2).

X_{CO} vs A_V : All models reproduce the observed increase of X_{CO} at $A_V \gtrsim 3$ mag, because they predict both the range of $N(\text{H}_2)$ and the saturation of I_{CO} comparable to our data. On the other hand, the uniform density model shows the decrease of X_{CO} at $A_V \lesssim 3$ mag much shallower than our data. This discrepancy mainly results from the less steep increase of I_{CO} predicted by the model at $A_V \lesssim 3$ mag.

Summary: While we do not perform a full parameter space search, our comparison between the “core-halo” and uniform density models is illustrative and demonstrates that the diffuse halo is essential for reproducing the following observed properties: the uniform $N(\text{HI})$ distribution, the H_2 -to- HI ratio for a given $N(\text{H})$, the sharp increase of I_{CO} and decrease of X_{CO} at $1 \text{ mag} \lesssim A_V \lesssim 3 \text{ mag}$. Considering that the uniform density model predicts the I_{CO} distribution extended toward smaller A_V , while producing the $N(\text{H}_2)$ distribution in reasonably good agreement with our data (Figures 12d and j), we expect that the neglect of the diffuse halo will result in the underestimation of the size of “CO-free” H_2 envelope.

7.2. Macroturbulent Time-dependent Model

7.2.1. Summary of the S11 Model

The S11 model is essentially comprised of two parts. The first part is a modified version of the ZEUS-MP MHD code (Stone & Norman 1992; Norman 2000). Gas in a periodic box is set to have a uniform density distribution and is driven by a turbulent velocity field with uniform power $1 \leq k \leq 2$ where k is the wavenumber. In addition, the magnetic field has initially orientation parallel to the z -axis, with a strength of $1.95 \mu\text{G}$. To model the chemical evolution of the gas, Glover & Mac Low (2007a,b), Glover et al. (2010), and Glover & Clark (2012) updated the ZEUS-MP MHD code with chemical reactions of several atomic and molecular species. The photodissociation of molecules by a radiation field is treated by the “six-ray approximation” method developed by Glover & Mac Low (2007a). The effect of self-gravity is not included. We refer to Glover & Mac Low (2007a,b), Glover et al (2010), and Glover & Clark (2012) for details on MHD, thermodynamics, and chemistry included in the S11 model. The second part is a three-dimensional radiative transfer code RADMC-3D (Dullemond et al. in prep)⁸. Once the simulated molecular cloud reaches a statistically steady state, RADMC-3D is executed to model molecular line emission (e.g., CO). To solve the population levels of atomic and molecular species, RADMC-3D implements the LVG method (Sobolev 1957), which has been shown to be a good approximation for molecular clouds (e.g., Ossenkopf 1997). We refer to Shetty et al. (2011a) for details on RADMC-3D.

The MHD simulation follows the evolution of an initially atomic gas in a $(20 \text{ pc})^3$ box with a numerical resolution of 512^3 . In this paper, we use the S11 model with the following input parameters: initial $n = 100 \text{ cm}^{-3}$, $G = 1 G'_0$, $\zeta = 10^{-17} \text{ s}^{-1}$, $Z = 1 Z_\odot$, and $\text{DGR} = 5.3 \times 10^{-22} \text{ mag cm}^2$. This simulation is essentially

⁸See <http://www.ita.uni-heidelberg.de/~dullemond/software/radmc-3d/>.

the same as the “n100 model” in S11 but has a higher numerical resolution and a simpler CO formation model based on Nelson & Langer (1999). We choose this particular simulation because it has a mass of $\sim 2 \times 10^4 M_{\odot}$, consistent with that of Perseus. The input parameters for the S11 model are reasonably close to what we expect for Perseus but not exactly the same as what we used for the modified W10 model. As it has been shown in S11 and Glover & Mac Low (2007b) that the simulated H_2 and CO column densities do not depend on small changes in G and ζ , this simulation would be appropriate for the comparison with our observations (Section 8.4.1 for details).

Compared to the modified W10 model, the final density distribution in the S11 model has a majority of the data points ($\sim 99\%$) with $n < 10^3 \text{ cm}^{-3}$, resulting in the small median density of $\sim 30 \text{ cm}^{-3}$. Another important difference between the modified W10 model and the S11 model is that H_2 formation in the S11 model does not achieve chemical equilibrium until the end of the simulation. For example, Glover et al. (2010) found from their MHD simulations that the H_2 abundance primarily depends on the time available for H_2 formation and shows no indication of chemical equilibrium up to $t \sim 20$ Myr. The gas will eventually become fully H_2 unless the molecular cloud is destroyed by stellar feedback such as photoevaporation by HII regions and protostellar outflows. On the other hand, the CO abundance is controlled by photodissociation and reaches chemical equilibrium within $t \sim 2$ Myr.

The final products of the S11 model include the $N(\text{HI})$, $N(\text{H}_2)$, and I_{CO} images obtained at $t \sim 5.7$ Myr. We smooth and regrid the simulated $N(\text{HI})$, $N(\text{H}_2)$, and I_{CO} images so that they have both a spatial resolution of 0.4 pc and a pixel size of 0.4 pc. Recently, Beaumont et al. (2013) compared the COMPLETE data of Perseus with the S11 model and found that the S11 model systematically overestimates $N(\text{H}_2)$ (e.g., Figure 5 of Beaumont et al. 2013). One of the possible explanations for this discrepancy is the different size between the simulation box and the individual regions in Perseus. Because the simulation box is larger than the individual regions in Perseus (20 pc vs $\sim 5\text{--}7$ pc), the integrated quantities $N(\text{HI})$, $N(\text{H}_2)$, and I_{CO} would need to be scaled. In the case of $N(\text{HI})$ and $N(\text{H}_2)$, the scaling is straightforward under the assumption of isotropic density distribution, which is appropriate for the S11 model⁹, and we simply need to account for the difference between the box and region sizes. However, estimating a proper scaling for I_{CO} is much more complicated because of the following reasons. First, the I_{CO} image was produced from the S11 model by integrating the CO brightness temperature, which was estimated by three-dimensional radiative transfer calculations, along a full radial velocity range. Second, the CO emission is optically thick in some parts of the simulation ($\sim 10\%$ of the volume). Re-running the simulation with a smaller box does not solve the problem as molecular cores/clouds form out of initially larger-scale diffuse ISM. We therefore take an approach of determining the optimal line of sight (LoS) depth that minimizes the difference between our observations and the S11 model by investigating the $N(\text{HI})$ and $N(\text{H}_2)$ images simultaneously. For the simulated I_{CO} image, on the other hand, we do not apply any scaling.

To do this, we estimate the difference between the observed mean and the simulated mean for each of $N(\text{HI})$ and $N(\text{H}_2)$ with varying LoS depths. For example, we divide the simulated $N(\text{HI})$ and $N(\text{H}_2)$ images by two to calculate the mean $N(\text{HI})$ and $N(\text{H}_2)$ for the simulation with the LoS depth of 10 pc. We then normalize the difference by the observed mean of each quantity and calculate the sum of the two normalized differences in quadrature. The results are shown in Figure 13 and we find that the LoS depth that minimizes

⁹We found that the assumption of isotropic density distribution is reasonable. For the optimal line of sight depth of 7 pc that minimizes the difference between our data and the S11 model, we derived three different versions of $N(\text{H})$ image by integrating the simulated number density cube for 7 pc but with three different intervals. These images were then compared with the image we derived by multiplying the original $N(\text{H})$ image from the S11 model by 7/20. The histograms of all four $N(\text{H})$ images were very similar with each other.

the difference between our data and the simulation products is 7 pc (Figure 13c). While the final quantity in Figure 13(c) has a broad minimum, it is encouraging that the estimated scale length is comparable to both the characteristic size of the five regions in Perseus and the total size of the slab for the “core-halo” model (Tables 1 and 2). As a double check that this scale length is appropriate, we use Larson’s law established for turbulent molecular clouds from both observations and MHD simulations: $\sigma_{\text{CO}} = (0.96 \pm 0.17)L_{\text{pc}}^{0.59 \pm 0.07}$ km s⁻¹ (Heyer & Brunt 2004). For a region size of 20 pc we expect $\sigma_{\text{CO}} \sim 6$ km s⁻¹, while for a region size of 7 pc we expect $\sigma_{\text{CO}} \sim 3$ km s⁻¹. This level of CO velocity dispersion is in agreement with what is shown in Figure 6, confirming that scaling the simulation products to the LoS depth of 7 pc is reasonable. In summary, when we compare our observations with the S11 model, we scale the simulated $N(\text{HI})$, $N(\text{H}_2)$, and $N(\text{H})$ images by multiplying them by 7/20 (Figures 14a, b, c, and Figures 15a, b). On the other hand, because of the uncertainty in I_{CO} scaling, we use the original I_{CO} image produced by the S11 model (Figure 14d and Figures 15c, d).

Finally, we apply the following thresholds to the simulated data to mimic the sensitivity limits of our observational data: $N(\text{H}_2) > 3.3 \times 10^{19}$ cm⁻² and $I_{\text{CO}} > 0.09$ K km s⁻¹ (our mean 1σ uncertainties calculated for the data points with $N(\text{H}_2) > 0$ cm⁻² and $I_{\text{CO}} > 0$ K km s⁻¹). This application of the thresholds to the S11 model is reasonable, considering the minimum $N(\text{H}_2) \sim 3.8 \times 10^{19}$ cm⁻² and $I_{\text{CO}} \sim 0.2$ K km s⁻¹ for the five regions in Perseus.

7.2.2. Comparison with Observations: Global Properties

We first compare our data with the S11 model by constructing normalized histograms of $N(\text{HI})$, $N(\text{H}_2)$, $N(\text{H})$, and I_{CO} in Figure 14. To construct the histograms, we use the data points with $N(\text{H}_2) > 0$ cm⁻² in Figure 2 (“All” histograms in black), as well as those shown in Figure 4 (“Subset” histograms in grey). While the grey histograms are limited to the regions where the CO emission is detected, the black histograms represent the whole Perseus cloud. The simulated data from the S11 model (smoothed, regridded, scaled for 7 pc, and the thresholds applied) are shown as green histograms. Note that the I_{CO} values from the S11 model are not scaled and therefore the green I_{CO} histogram likely represents the upper limit of actual histogram for sub-regions with a size of ~ 7 pc (indicated as an arrow). Because the simulated data (except for I_{CO}) are scaled to match the properties of the five regions and the thresholds applied to the S11 model are comparable to the minimum $N(\text{H}_2)$ and I_{CO} values of the five regions, the green histograms can be directly compared with the grey histograms. In comparison between our data and the S11 model, we find the following.

First, the black and grey $N(\text{HI})$ histograms are nearly identical. This results from the small variation in $N(\text{HI})$ across the whole Perseus cloud, as discussed in Section 2.1. The green histogram, on the other hand, has a peak at a factor of ~ 2 smaller $N(\text{HI})$ and even more importantly a factor of ~ 6 broader distribution than the observed data (the black and grey histograms).

Second, the grey and green $N(\text{H}_2)$ histograms agree very well: both peak at a similar $N(\text{H}_2)$, have a similar width, and show a lognormal-like distribution. The black histogram, on the other hand, is broader and has a tail toward small $N(\text{H}_2)$. The difference between the black and grey histograms results from the existence of H_2 beyond the CO spatial coverage (e.g., “CO-dark” H_2 discussed in Lee et al. 2012).

Third, the green $N(\text{H})$ histogram peaks at a similar $N(\text{H})$ compared to the grey histogram, while showing a broader (a factor of ~ 2) and lognormal-like distribution. The simulated distribution is broader mainly because the simulated $N(\text{HI})$ has a greater range than what is observed. The black and grey histograms,

on the other hand, have a tail toward $N(\text{H}) \gtrsim 10^{21.4} \sim 2.5 \times 10^{21} \text{ cm}^{-2}$. This tail is consistent with Kainulainen et al. (2009), who found a deviation from the lognormal distribution at $A_V \gtrsim 3 \text{ mag}$ for Perseus (corresponding to $N(\text{H}) \sim 2.7 \times 10^{21} \text{ cm}^{-2}$ with $\text{DGR} = 1.1 \times 10^{-21} \text{ mag cm}^2$) and interpreted it as a result of self-gravity.

Lastly, because the simulated I_{CO} is not scaled for the LoS depth of 7 pc, we do not compare the exact shapes of the green and grey histograms but emphasize that the simulated I_{CO} becomes comparable to the observed I_{CO} only if we use the whole simulation box of 20 pc.

In summary, we find that the scaled S11 model reproduces the observed range of $N(\text{H}_2)$ very well. While the predicted $N(\text{HI})$ has a relatively similar mean value compared to the observed $N(\text{HI})$, it has a broader distribution and this leads to a broader range of $N(\text{H})$ in the simulation. The I_{CO} values from the S11 model, on the other hand, cannot be properly compared with our observations because of the nontrivial scaling of I_{CO} with the LoS depth. However, we find that the simulated I_{CO} is similar with the observed I_{CO} only when the CO emission is integrated for the full simulation box of 20 pc.

7.2.3. Comparison with Observations: R_{H_2} and X_{CO}

We plot $N(\text{HI})$ against $N(\text{H})$ for each dark and star-forming region and show predictions from the S11 model (smoothed, regridded, scaled for 7 pc, and the thresholds applied) in Figure 15(a). While the observed $N(\text{HI}) \sim 9 \times 10^{20} \text{ cm}^{-2}$ is in the range of the predicted $N(\text{HI})$, the relation between $N(\text{HI})$ and $N(\text{H})$ in the S11 model is different from what we find in Perseus: not only does the simulated $N(\text{HI})$ have a broader distribution, but the S11 model predicts a factor of ~ 7 increase of $N(\text{HI})$ for the range of $N(\text{H})$ in Perseus, where we observe less than a factor of 2 variation in $N(\text{HI})$. This suggests that $N(\text{HI})$ linearly correlates with $N(\text{H})$ in the S11 model and we indeed estimate Pearson’s linear correlation coefficient $r_p \sim 0.8$.

In addition, the S11 model predicts a factor of ~ 2 smaller $N(\text{HI})$ for a given $N(\text{H})$ on average. As a result, R_{H_2} is slightly larger in the S11 model for a given $N(\text{H})$ and increases with $N(\text{H})$ with a slope smaller than what we observe (Figure 15b). While our observations show $R_{\text{H}_2} < 1$ for the outskirts of the five regions, the simulation has $R_{\text{H}_2} > 1$ everywhere, even for the regions with small $n < 10^2 \text{ cm}^{-3}$.

Next, we plot the observed I_{CO} as a function of A_V and show the S11 model in Figure 15(c). As discussed in Section 7.2.1, the simulated $N(\text{HI})$ and $N(\text{H}_2)$ data can be scaled for the five regions in Perseus, while the simulated I_{CO} data cannot. To properly examine the relation between I_{CO} and A_V in the S11 model, therefore, we show the predicted I_{CO} vs A_V profile without applying the scaling and the thresholds and focus on only the general shape of the profile. We find that the S11 model describes the relation between I_{CO} and A_V reasonably well: a steep increase of I_{CO} at small A_V and a hint of the saturation of I_{CO} at large A_V . Interestingly, the S11 model predicts that I_{CO} increases with a large scatter at small A_V .

Finally, we show the X_{CO} vs A_V profile for each dark and star-forming region in Figure 15(d) with the S11 model. As in Figure 15(c), the unscaled $N(\text{HI})$, $N(\text{H}_2)$, and I_{CO} data are used for this comparison. We find that the S11 model predicts a sharp decrease of X_{CO} at small A_V and a gradual increase of X_{CO} at large A_V . While a quantitative comparison is not possible without scaling, the simulated data show the characteristic relation between X_{CO} and A_V in broad agreement with the observational data (particularly for IC348 and B1E/B1). This is consistent with Shetty et al. (2011a), who performed a number of MHD simulations ($n = 100, 300, 1000 \text{ cm}^{-3}$ and $Z = 0.1, 0.3, 1 Z_\odot$) and found a steep decrease of X_{CO} at $A_V \lesssim 7 \text{ mag}$ and a steady increase of X_{CO} at $A_V \gtrsim 7 \text{ mag}$ for all simulations probing a large range of interstellar

environments. Relative to the observations, we find that the simulated X_{CO} shows a significantly larger scatter at small A_V , while the scatter becomes more comparable to what is found in the observations at the high end of the A_V range.

8. Discussion

8.1. X_{CO} in Perseus and Comparison with Previous Studies

In their recent review, Bolatto et al. (2013) showed that there is some degree of uniformity among the X_{CO} values in the Milky Way obtained from a variety of observational methods. Essentially, the typical value for the Milky Way is $X_{\text{CO}} \sim 2 \times 10^{20}$ and is known within a factor of ~ 2 . We, on the other hand, found that the dark and star-forming regions in Perseus have $\langle X_{\text{CO}} \rangle$ at least five times smaller than the typical value. In Appendix, we provide a detailed comparison with two previous studies, Dame et al. (2001) and Pineda et al. (2008), to understand the reasons behind such a significant difference. We summarize our findings here.

We find three potential sources responsible for the difference: the different resolution of I_{CO} and $N(\text{H}_2)$ images used to derive X_{CO} , the application of different DGR, and the treatment of HI in deriving $N(\text{H}_2)$. For example, Dame et al. (2001) estimated $\langle X_{\text{CO,Dame}} \rangle \sim 1.2 \times 10^{20}$ for Perseus, which is a factor of ~ 4 larger than our $\langle X_{\text{CO}} \rangle \sim 3 \times 10^{19}$, by combining I_{CO} from the CfA survey with $N(\text{H}_2)$ derived using the $E(B - V)$ data from Schlegel et al. (1998) and the HI data from the Leiden-Argentine-Bonn (LAB) Survey (Kalberla et al. 2005). Their study, as well as other large-scale studies of X_{CO} in the Milky Way (e.g., Abdo et al. 2010; Paradis et al. 2012), is at $36'$ resolution, mainly limited by the LAB HI data. In comparison between our original X_{CO} at $4.3'$ resolution and our X_{CO} smoothed to $36'$ resolution, we find that spatial smoothing results in a factor of ~ 1.5 increase in $\langle X_{\text{CO}} \rangle$. Considering a factor of ~ 8 decrease in angular resolution, the effect of resolution on the estimation of $\langle X_{\text{CO}} \rangle$ appears to be mild and is within the accepted uncertainties, although this would be likely more significant when comparing extragalactic observations on $\sim \text{kpc}$ scales. We then find that the rest of the difference between our $\langle X_{\text{CO}} \rangle$ and $\langle X_{\text{CO,Dame}} \rangle$ can be explained by the difference in DGR. While both studies measured DGR, Dame et al. (2001) calculated $N(\text{HI})$ along a whole line of sight (while we focused on the velocity range for Perseus only) and estimated DGR using the images smoothed to 10° resolution (while we had $4.3'$ resolution). The DGR effect is slightly larger than the resolution effect (a factor of ~ 1.8) and these two factors together account for most of the difference between our study and Dame et al. (2001).

In the case of Pineda et al. (2008), angular resolution is not an issue because essentially the same A_V and I_{CO} data were used. However, they estimated $X_{\text{CO,Pineda}} \sim 1.4 \times 10^{20}$ for Perseus. Their methodology for deriving X_{CO} is different from our study mainly in two ways. First, they assumed that the $N(\text{HI})$ contribution to A_V is insignificant and therefore did not consider it. Second, they adopted the typical DGR for the Milky Way $= 5.3 \times 10^{-22} \text{ mag cm}^2$ (Bohlin et al. 1978). In contrast, we accounted for the $N(\text{HI})$ contribution and estimated $\text{DGR} = 1.1 \times 10^{-21} \text{ mag cm}^2$ (Lee et al. 2012). In Appendix, we show that we estimate $\langle X_{\text{CO}} \rangle \sim 1 \times 10^{20}$, which is comparable to $X_{\text{CO,Pineda}}$, when we follow the methodology of Pineda et al. (2008). In addition, we find that the application of each of the two assumptions made by Pineda et al. (2008) results in a factor of ~ 2 difference in $\langle X_{\text{CO}} \rangle$, altogether explaining the difference between our $\langle X_{\text{CO}} \rangle$ and $X_{\text{CO,Pineda}}$.

Our detailed comparison with Dame et al. (2001) and Pineda et al. (2008) shows that different resolutions and methodologies for deriving X_{CO} can result in a difference in X_{CO} by up to a factor of ~ 4 , even

for the same method of X_{CO} determination (X_{CO} based on dust emission/absorption in this case). Other methods of X_{CO} determination, e.g., X_{CO} based on the Virial technique and γ -ray observations, have their own assumptions. This clearly suggests the difficulty in comparing X_{CO} between molecular clouds and/or galaxies when different observational methods are used, as pointed out by Bolatto et al. (2013) as well. The relatively uniform value of X_{CO} for the Milky Way found from many studies with various resolutions and methodologies, therefore, appears puzzling.

8.2. X_{CO} in Molecular Clouds

In Section 6.3, we focused on the individual dark and star-forming regions in Perseus and found significant spatial variations in X_{CO} . Specifically, X_{CO} varies by up to a factor of ~ 100 within a single region with a size of ~ 6 – 7 pc. Our investigation of the large-scale trends in G and σ_{CO} (Section 6.1) and our comparison with the modified W10 model (Section 7.1) suggest that changes in physical parameters are responsible for the variations in X_{CO} observed both within the individual regions and between the different regions.

While X_{CO} shows significant variations across the cloud, we found that there is a characteristic dependence of X_{CO} on A_V (particularly evident for IC348 and B1E/B1): a steep decrease of X_{CO} at $A_V \lesssim 3$ mag and a moderate increase of X_{CO} at $A_V \gtrsim 3$ mag. This relation between X_{CO} and A_V appears to result from the strong dependence of I_{CO} on A_V . The location at which most carbon is locked in CO primarily depends on dust shielding (e.g., W10; Glover & Mac Low 2011). Once dust shielding becomes sufficiently strong to prevent photodissociation ($A_V \gtrsim 1$ mag in Perseus), the CO abundance and emission strength sharply rise and this could result in decreasing X_{CO} with A_V . I_{CO} then saturates to a certain value because the CO emission becomes optically thick with increasing depths ($A_V \gtrsim 3$ mag in Perseus) and this could result in increasing X_{CO} with A_V . These results suggest that CO is a poor tracer of H_2 for those regions where dust shielding is not strong enough to prevent photodissociation, e.g., low-metallicity environments (e.g., Leroy et al. 2007, 2009, 2011; Cormier et al. 2014). In addition, CO is unreliable for those regions where the CO emission is optically thick, because it provides only a lower limit on $N(\text{H}_2)$.

Overall, our study suggests that one cannot adopt a single X_{CO} to derive the $N(\text{H}_2)$ distribution across a resolved molecular cloud. The limited dynamic range of CO as a tracer of H_2 and the complex dependence of X_{CO} on various physical parameters hamper the derivation of the accurate $N(\text{H}_2)$ distribution. On the other hand, calculation of the H_2 mass over the CO-observed area, $M(\text{H}_2)_{\text{CO}}$, appears to be less affected by variations in physical parameters. For example, we estimate $M(\text{H}_2)_{\text{CO}} = (1799.8 \pm 3.2) M_{\odot}$ over the COMPLETE CO spatial coverage. If we derive $M(\text{H}_2)_{\text{CO}}$ using our $\langle X_{\text{CO}} \rangle$, we find $M(\text{H}_2, X_{\text{CO}})_{\text{CO}} = (1814.1 \pm 0.2) M_{\odot}$. These two estimates are comparable for Perseus, mainly because a large fraction of the data points ($\sim 60\%$) has X_{CO} different from our $\langle X_{\text{CO}} \rangle$ within a factor of ~ 2 .

The agreement between the observed X_{CO} in Perseus and the model predictions (in particular for the PDR model) suggests that a theory-based X_{CO} could be used to estimate $M(\text{H}_2)_{\text{CO}}$ for a molecular cloud. Once theoretical models, e.g., PDR and MHD models, are thoroughly tested against observations of molecular clouds in diverse environments, they will be able to provide predictions over a wide range of physical conditions. One then can search a large parameter space to select the most appropriate X_{CO} for a target molecular cloud based on reasonable constraints on physical parameters. Note, however, that the total H_2 mass of the cloud would be still uncertain if there is significant “CO-dark” H_2 outside the CO-observed area.

8.3. Insights from the Microturbulent Time-independent Model

The good agreement between our data and the modified W10 model with the “core-halo” structure (Section 7.1.2) suggests that the main assumptions of the model, e.g., H₂/CO formation in chemical equilibrium, the microturbulent approximation for CO spectral line formation, and the “core-halo” density distribution, are valid for Perseus on ~ 0.4 pc scales. This result is consistent with Lee et al. (2012), who found that $N(\text{HI})$ and $N(\text{H}_2)$ in Perseus conform to the time-independent H₂ formation model by K09. We now turn to a couple of interesting aspects of the modified W10 model and discuss their implications.

8.3.1. The Importance of Diffuse HI Halo for H₂ and CO Formation

The modified W10 model that is comparable to the observations of Perseus uses the “core-halo” structure motivated by previous studies of molecular clouds (Section 7.1.1). We showed that the model with a uniform density distribution predicts $N(\text{HI})$ much smaller than the uniform $N(\text{HI}) \sim 9 \times 10^{20} \text{ cm}^{-2}$ measured across Perseus. The uniform density model with the largest density $n = 10^4 \text{ cm}^{-3}$ predicts the smallest $N(\text{HI})$, up to a factor of ~ 160 smaller than what is observed. The main reason is that in the uniform density model H₂ self-shielding alone counteracts H₂ photodissociation by LW photons. Traditionally, it has been known that G/n determines whether H₂ self-shielding or dust shielding is more important for H₂ formation and controls the location of the transition from HI to H₂ in a PDR (e.g., Hollenbach & Tielens 1997). With $G = 0.5 G'_0$ and $n = 10^3 \text{ cm}^{-3}$ in the uniform density model, G/n is $5 \times 10^{-4} \text{ cm}^3$, small enough that dust shielding is negligible. In this case, most of the HI is converted into H₂ because of the strong H₂ self-shielding. On the other hand, the “core-halo” model with $n_{\text{core}} = 10^3 \text{ cm}^{-3}$ and $n_{\text{halo}} = 40 \text{ cm}^{-3}$ has $G/n_{\text{halo}} \sim 0.01 \text{ cm}^3$ in the cloud outskirts. This increased G/n makes H₂ self-shielding less important for H₂ formation and as a result, the gas remains atomic with $N(\text{HI}) \sim 9 \times 10^{20} \text{ cm}^{-2}$.

The fact that the modified W10 model needs a diffuse HI halo to reproduce the observed $N(\text{HI})$ suggests that dust shielding is important for H₂ formation in Perseus. This importance of dust shielding is consistent with what Lee et al. (2012) found from their comparison with the K09 model. The K09 model investigates the structure of a PDR in a spherical cloud based on H₂ formation in chemical equilibrium and predicts the following variable as one of the key parameters that determine the location of the transition from HI to H₂:

$$\chi = 2.3 \frac{(1 + 3.1Z'^{0.365})}{\phi_{\text{CNM}}}, \quad (3)$$

where Z' is the metallicity normalized to the solar neighborhood value and ϕ_{CNM} is the ratio of the actual CNM density to the minimum CNM density at which the CNM exists in pressure balance with the warm neutral medium (WNM). This χ is the ratio of the rate at which LW photons are absorbed by dust grains (dust shielding) to the rate at which they are absorbed by H₂ (H₂ self-shielding) and is conceptually similar to G/n . K09 predicts $\chi \sim 1$ in all galaxies where the pressure balance between the CNM and the WNM is valid, suggesting that dust shielding and H₂ self-shielding are equally important for H₂ formation. By fitting the K09 model to the observed R_{H_2} vs $\Sigma_{\text{HI}+\Sigma_{\text{H}_2}}$ profiles, Lee et al. (2012) indeed found $\chi \sim 1$ for Perseus.

In the modified W10 model, a diffuse HI halo is also required to reproduce the observed steep increase of I_{CO} at $A_V \gtrsim 1$ mag and sharp decrease of X_{CO} at $A_V \lesssim 3$ mag (Section 7.1.3). The uniform density model predicts the shallower increase of I_{CO} at smaller $A_V \gtrsim 0.6$ mag, suggesting a less sharp transition from CII/CI to CO located closer to the surface of the gas slab. The more extended CO distribution eventually

results in the reduced “CO-free” H₂ envelope and therefore the uniform density model with $n = 10^4 \text{ cm}^{-3}$ would have the smallest amount of “CO-dark” H₂. The CO distribution deep inside of the gas slab, on the other hand, does not appear to be affected by the presence of the diffuse HI halo because of the saturation of I_{CO} .

Even though the modified W10 model with the “core-halo” structure reproduces the observed $N(\text{HI})$, $N(\text{H}_2)$, and I_{CO} distributions, the agreement is likely to remain only if the halo density is not significantly larger than 40 cm^{-3} . The current density $n_{\text{halo}} = 40 \text{ cm}^{-3}$ originates from the theoretical (e.g., Wolfire et al. 2003) and observational (e.g., Heiles & Troland 2003) properties of the CNM. While large HI envelopes associated with molecular clouds have been frequently observed (e.g., Knapp 1974; Wannier et al. 1983, 1991; Reach et al. 1994; Rogers et al. 1995; Williams & Maddalena 1996; Imara & Blitz 2011; Lee et al. 2012), a number of fundamental questions still remain to be answered. For example, what are the physical properties of the HI halos, such as density, temperature, and pressure? What is the ratio of the CNM to the WNM in the halos? Is there any correlation between the ratio and the H₂ abundance/star formation? Are the halos expanding or infalling? The high-resolution HI data from the GALFA-HI survey will be valuable for future studies of the extended HI halos around Galactic molecular clouds in a wide range of interstellar environments. Finally, further comparisons between observations and theoretical models will be important to fully constrain the parameter space and density structure of the HI halos.

8.3.2. Validity of Steady State and Equilibrium Chemistry

The timescale of H₂ formation on dust grains, t_{H_2} , dominates chemical timescales of PDRs (e.g., Hollenbach & Tielens 1997). For the modified W10 model with the “core-halo” structure, dense regions have $n_{\text{core}} \gtrsim 10^3 \text{ cm}^{-3}$ where gas is completely molecular ($n_{\text{H}_2} \sim 0.5n$). In this case, $t_{\text{H}_2} = 0.5/\mathcal{R}n_{\text{core}} \lesssim 0.5 \text{ Myr}$, where $\mathcal{R} = 3 \times 10^{-17} \text{ cm}^3 \text{ s}^{-1}$ is the rate coefficient for H₂ formation (Wolfire et al. 2008). In diffuse regions with $n_{\text{halo}} = 40 \text{ cm}^{-3}$, on the other hand, gas is mostly atomic ($n_{\text{H}_2} \sim 0.1n$) and therefore $t_{\text{H}_2} = 0.1/\mathcal{R}n_{\text{halo}} \sim 2.6 \text{ Myr}$. Because t_{H_2} of the model is well within the expected age of Perseus, $t_{\text{age}} \sim 10 \text{ Myr}$, the assumption of chemical equilibrium is valid. In other words, Perseus is old enough to reach chemical equilibrium and therefore it is not surprising that the equilibrium chemistry model (W10) fits our observations very well.

However, for steady state chemistry to be valid, $t_{\text{H}_2} \lesssim t_{\text{age}}$ is not enough: t_{H_2} should be short compared to the dynamical timescale of a molecular cloud, t_{dyn} . For Perseus, this requires $t_{\text{dyn}} \gtrsim 3 \text{ Myr}$. As a rough estimate, we calculate a crossing timescale, $t_{\text{cross}} = L/\sigma \sim 10 \text{ pc}/1.8 \text{ km s}^{-1} \sim 6 \text{ Myr}$, where we choose L as the characteristic size of the individual regions in Perseus and σ as the mean CO velocity dispersion. This $t_{\text{cross}} \sim 6 \text{ Myr}$ satisfies the condition for $t_{\text{dyn}} \gtrsim 3 \text{ Myr}$. However, many dynamical processes are involved with the formation and evolution of molecular clouds (e.g., cloud-cloud collisions, spiral shocks, stellar feedback; Mac Low & Klessen 2004; Mckee & Ostriker 2007) and therefore it is difficult to pin down the exact process that is most relevant for the formation of molecular gas. The good agreement between our data and the modified W10 model with the “core-halo” structure suggests that the characteristic t_{dyn} for the formation of molecular gas in Perseus should be $\gtrsim 3 \text{ Myr}$.

8.4. Insights from the Macroturbulent Time-dependent Model

8.4.1. The Choice of the Input Parameters in the MHD Simulation

In Section 7.2.2, we found that the scaled S11 model predicts $N(\text{H}_2)$ comparable to the estimated $N(\text{H}_2)$ in Perseus. This excellent agreement will likely hold even if some of the input parameters slightly change. For example, the S11 model was run with $G = 1 G'_0$ and this is a factor of ~ 2 stronger than what we measure across Perseus. Considering that S11 found no considerable difference in $N(\text{H}_2)$ for their models with $G = 1 G'_0$ and $10 G'_0$ (Section 3.1 of S11), however, decreasing G from $1 G'_0$ to $0.5 G'_0$ to match the property of Perseus will not make a significant change in $N(\text{H}_2)$. In addition, increasing ζ from 10^{-17} s^{-1} to 10^{-16} s^{-1} to be consistent with the modified W10 model will not affect $N(\text{H}_2)$ very much, based on the fact that Glover & Mac Low (2007b) found a negligible change in $N(\text{H}_2)$ when ζ increased from 10^{-17} s^{-1} to 10^{-15} s^{-1} in their MHD simulation with initial $n = 100 \text{ cm}^{-3}$ (Section 6.3 of Glover & Mac Low 2007b). Increasing DGR from $5.3 \times 10^{-22} \text{ mag cm}^2$ to $1.1 \times 10^{-21} \text{ mag cm}^2$ for Perseus will lead to more rapid H_2 formation, but the model with the increased DGR will not be substantially different from the current S11 model since the S11 model becomes H_2 -dominated rapidly by $t \sim 3 \text{ Myr}$ (Figure 7 of Glover & Mac Low 2011). Finally, the extension of the simulation run up to $t \sim 10 \text{ Myr}$, comparable to the age of Perseus, will not significantly increase $N(\text{H}_2)$, considering that Glover & Mac Low (2011) found only a factor of ~ 1.3 increase of the mass-weighted mean H_2 abundance from $t \sim 5 \text{ Myr}$ to $t \sim 10 \text{ Myr}$ for their MHD simulation with initial $n = 100 \text{ cm}^{-3}$ (Section 3.3 of Glover & Mac Low 2011).

Similarly, small changes in the model parameters will likely make no substantial difference in I_{CO} . For example, S11 showed that increasing G from $1 G'_0$ to $10 G'_0$ does not change I_{CO} for those regions where CO is well shielded against the radiation field (Section 3.1 of S11). Therefore, decreasing G from $1 G'_0$ to $0.5 G'_0$ will make only a minor change in I_{CO} at large column densities. Increasing the current DGR of $5.3 \times 10^{-22} \text{ mag cm}^2$ by a factor of ~ 2 will cause more rapid CO formation, but I_{CO} will not be significantly influenced because CO formation in the S11 model reaches chemical equilibrium rapidly by $t \sim 2 \text{ Myr}$. Lastly, we do not expect that running the S11 model up to $t \sim 10 \text{ Myr}$ drastically increases I_{CO} , considering that the MHD simulation with initial $n = 100 \text{ cm}^{-2}$ in Glover & Mac Low (2011) predicts only a factor of ~ 2 increase of the mass-weighted mean CO abundance from $t \sim 5 \text{ Myr}$ to $t \sim 10 \text{ Myr}$ (Section 3.3 of Glover & Mac Low 2011). Note that changes in CO abundance at $t > 2 \text{ Myr}$ are stochastic fluctuations after chemical equilibrium is achieved.

We therefore conclude that the input parameters used in the S11 model are reasonable for the comparison with the observations of Perseus and small (a factor of few) changes in the input parameters will not result in significant changes in $N(\text{HI})$, $N(\text{H}_2)$, and I_{CO} . Considering that Perseus has most likely reached chemical equilibrium, it provides a suitable testbed for investigating whether results from the time-dependent MHD simulation converge to the time-independent PDR model for molecular clouds that are evolved enough.

8.4.2. The Role of Turbulence in H_2 and CO Formation

As shown in Section 7.2.2, the scaled S11 model produces the $N(\text{H}_2)$ distribution in excellent agreement with our observations as well as the modified W10 model. This suggests that the time-dependent H_2 formation model (S11) is consistent with the time-independent H_2 formation model (W10) for a low-mass, old molecular cloud such as Perseus. Our result agrees with Krumholz & Gnedin (2011), who found that time-dependent effects on H_2 formation become important only at extremely low metallicities $Z \lesssim 10^{-2} Z_\odot$.

While the median $N(\text{HI})$ in the S11 model is also in reasonably good agreement with the observations, the simulated $N(\text{HI})$ distribution is a factor of ~ 6 broader than the observed one and particularly shows a more extended tail toward small $N(\text{HI}) \lesssim 3 \times 10^{20} \text{ cm}^{-2}$. This broad $N(\text{HI})$ distribution in the MHD simulation likely results from strong compressions and rarefactions by turbulence and the predicted $N(\text{HI})$ is on average a factor of ~ 2 smaller than the observed $N(\text{HI})$ for a given $N(\text{H})$. The discrepancy becomes significant at small $N(\text{H}) \sim 10^{21} \text{ cm}^{-2}$, where the S11 model underestimates $N(\text{HI})$ by up to a factor of ~ 10 . Finally, the S11 model predicts that $N(\text{HI})$ increases with $N(\text{H})$, suggesting no minimum $N(\text{HI})$ beyond which the rest of hydrogen is converted into H_2 . In the modified W10 model with the “core-halo” structure, on the other hand, the diffuse halo remains atomic with $N(\text{HI}) \sim 9 \times 10^{20} \text{ cm}^{-2}$ and the dense core is fully converted into H_2 . Clearly, this discrepancy in $N(\text{HI})$ between the simulation and the observations is significant and interesting. One potential avenue in exploring this in the future is by using a mixture of neutral phases for initial conditions, mimicing in some way the “core-halo” structure in the modified W10 model.

In the case of I_{CO} , we could not properly compare the S11 model with our observations because of the nontrivial scaling of I_{CO} for different line of sight depths. Instead, we found that the simulated I_{CO} becomes comparable to the observed I_{CO} only if the CO emission is integrated for the full simulation box of 20 pc. This suggests that the S11 model likely underestimates I_{CO} for the conditions relevant to Perseus. Interestingly, we estimate $N(\text{CO}) \sim 1 \times 10^{17} \text{ cm}^{-2}$ for B5, IC348, B1, and NGC1333 by using the $^{13}\text{CO}(J = 1 \rightarrow 0)$ excitation temperatures, optical depths, and integrated intensities provided by Pineda et al. (2008) and assuming $N(\text{CO}) = 76N(^{13}\text{CO})$ (Lequeux 2005). This value is in reasonably good agreement with the simulated mean $N(\text{CO}) \sim 5 \times 10^{16} \text{ cm}^{-2}$ (calculated from the smoothed, regridded, scaled, and thresholds applied S11 model)¹⁰. This comparison suggests that the potential discrepancy in I_{CO} between the observations and the S11 model would result from the radiative transfer calculations and/or the difference in velocity range. The velocity range of the CO emission, Δv , directly affects I_{CO} via $I_{\text{CO}} = \int T_{\text{B}} dv$ and a smaller Δv would result in a smaller I_{CO} for the same T_{B} .

While we could not compare specific I_{CO} values predicted by the S11 model with our observations, we found that the S11 model reproduces the observed shape of the I_{CO} vs A_V profiles reasonably well. This suggests that penetration of UV photons into the ISM and (dust and self-) shielding against the ISRF are relatively well captured in the CO formation process by S11. In addition, we noticed that I_{CO} has a much larger scatter at small A_V . This could result from large density fluctuations in the turbulent medium. The gas in the S11 model would be strongly compressed and rarefied by turbulence and the gas density at a given A_V can vary over several orders of magnitude (e.g., Figure 14 of Glover et al. 2010). In this case, CO can form in dense clumps even at small A_V and I_{CO} therefore shows a large scatter. This scatter is reduced at large A_V where I_{CO} eventually saturates. Finally, turbulent mixing could spread the CO distribution, contributing to the large scatter of I_{CO} .

In general, our study shows that the scaled MHD simulation by S11 is successful in reproducing $N(\text{H}_2)$ in Perseus, which is a low-mass, old molecular cloud most likely in chemical equilibrium. On the other hand, future model adjustments are required to better match the observed $N(\text{HI})$ and I_{CO} . We have revealed two important areas of future attention: (1) the role of diffuse halos in the formation of molecular gas and (2) the effect of density fluctuations and turbulent mixing in the spatial distribution of molecular gas. To investigate these two issues, we plan to compare observations of several Galactic molecular clouds with MHD simulations that explore different fractions of neutral phases and a varying degree of turbulence as initial

¹⁰As S11 did not perform any radiative transfer calculations to produce the CO number density cube, it is appropriate to scale the simulated $N(\text{CO})$.

conditions. In particular, our future work will include molecular clouds less evolved and/or forming more massive stars (therefore more turbulent) than Perseus, where the difference between the MHD and PDR models is likely to be more pronounced.

9. Summary

In this paper, we combine high-resolution H_2 and CO measurements to investigate X_{CO} across the Perseus molecular cloud. We derive the X_{CO} image at ~ 0.4 pc spatial resolution by using $N(H_2)$ estimated by Lee et al. (2012) and I_{CO} provided by the COMPLETE survey. We examine the large-scale spatial variations in X_{CO} across the cloud and their correlations with local ISM conditions. In addition, we focus on the characteristic dependence of X_{CO} on A_V .

The $N(HI)$, $N(H_2)$, I_{CO} , and X_{CO} images allow us to test two theoretical models of H_2 and CO formation: the modified W10 model (“microturbulent time-independent model”) and the S11 model (“macro-turbulent time-dependent model”). For several dark and star-forming regions in Perseus (B5, B1E/B1, L1448, IC348, and NGC1333), we investigate $N(HI)$ vs $N(H)$, R_{H_2} vs $N(H)$, I_{CO} vs A_V , and X_{CO} vs A_V and compare the results with model predictions. We summarize our main results as follows.

- (1) We derive $\langle X_{CO} \rangle \sim 3 \times 10^{19}$ for Perseus. This value is a factor of ~ 4 smaller than the previous estimate of $X_{CO} \sim 1 \times 10^{20}$ for the same cloud (Dame et al. 2001; Pineda et al. 2008) and the discrepancy mainly results from different resolutions, DGRs, and our consideration of $N(HI)$ in deriving $N(H_2)$.
- (2) We find a factor of ~ 3 region-to-region variations in X_{CO} . The northeastern part of Perseus (B5 and IC348) has on average larger X_{CO} than the southwestern part (B1E/B1, NGC1333, and L1448). This could be explained by a stronger G and/or a smaller σ_{CO} in the northeastern part, although the correlations between X_{CO} and G/σ_{CO} are mild. Additionally, variations in n and/or A_V could contribute to the observed regional variations in X_{CO} . Within the individual dark and star-forming regions with a size of ~ 6 – 7 pc, X_{CO} varies up to a factor of ~ 100 .
- (3) The observed X_{CO} vs A_V profiles show two characteristic features: a steep decrease of X_{CO} at small A_V and a gradual increase of X_{CO} at large A_V . Among the five dark and star-forming regions, IC348 and B1E/B1 clearly show the transition from decreasing to increasing X_{CO} at $A_V \sim 3$ mag.
- (4) The modified W10 model with the “core-halo” density distribution reproduces the observed X_{CO} vs A_V profiles, particularly well for IC348 and B1E/B1. In addition, the model predicts a nearly constant $N(HI) \sim 9 \times 10^{20} \text{ cm}^{-2}$ and a linear increase of R_{H_2} with $N(H)$, both consistent with what we find in Perseus.
- (5) The modified W10 model with the uniform density distribution reproduces the observed $N(H_2)$ reasonably well but underestimates $N(HI)$ by a factor of ~ 10 – 160 . As a result, the model overestimates R_{H_2} for a given $N(H)$ by up to a factor of ~ 300 . In addition, while matching the observed saturation of I_{CO} at $A_V \gtrsim 3$ mag, the model predicts a more gradual increase of I_{CO} at $A_V \lesssim 3$ mag. This results in the X_{CO} vs A_V profile shallower than the observations at $A_V \lesssim 3$ mag.
- (6) The scaled S11 model predicts $N(H_2)$ in excellent agreement with what we estimate in Perseus. However, $N(HI)$ increases with $N(H)$ by a factor of ~ 7 in the model and this is in contrast with the observed small variation of $N(HI)$ with $N(H)$ (less than a factor of 2). While we do not compare specific I_{CO} values in the S11 model with the observed I_{CO} due to a complex issue of scaling I_{CO} for different line of sight depths, we stress that the simulated I_{CO} becomes comparable only when the CO emission is integrated along the full simulation box of 20 pc, suggesting that the model likely underestimates I_{CO} for the conditions relevant to Perseus. In addition, we find that the S11 model reproduces the observed

shapes of I_{CO} vs A_V and X_{CO} vs A_V profiles reasonably well but with a large scatter particularly at small A_V .

Our study shows that X_{CO} can vary by up to a factor of ~ 100 on ~ 0.4 pc scales and depends on local ISM conditions such as G , σ_{CO} , n , and A_V . The characteristic relation of X_{CO} with A_V is mainly driven by how I_{CO} varies with A_V . At small A_V , X_{CO} steeply decreases with A_V , likely because CO becomes sufficiently shielded against photodissociation and I_{CO} sharply increases. X_{CO} then gradually increases with A_V , likely due to the saturation of I_{CO} . Our results observationally confirm previous theoretical predictions of the X_{CO} vs A_V profile for the first time. However, the precise details of the X_{CO} vs A_V profile, e.g., the location where the transition from decreasing to increasing X_{CO} occurs, the slopes of the decreasing and increasing portions, etc., again depend on local environmental parameters (e.g., Taylor et al. 1993; Bell et al. 2006; Shetty et al. 2011a). In general, our results suggest that a single X_{CO} cannot be used to derive the spatial distribution of $N(\text{H}_2)$ across a molecular cloud.

The detailed comparison between our high-resolution data and theory provides important insights into H_2 and CO formation in molecular clouds. For example, the good agreement we found with the modified W10 model suggests that the steady state and equilibrium chemistry and the microturbulent approximation for CO spectral line formation and cooling work well for Perseus on ~ 0.4 pc scales. Perseus appears to be old enough to achieve chemical equilibrium and the timescale of the dynamical process(es) most relevant for the formation of molecular gas is likely $\gtrsim 3$ Myr. However, the good agreement with the model is achieved only if the density distribution has a diffuse halo component. In the modified W10 model, the halo provides dust shielding against H_2 and CO photodissociation and is essential to reproduce the observed $N(\text{HI})$, R_{H_2} , I_{CO} , and X_{CO} distributions. While our results indicate the importance of the diffuse HI halo for the distributions of two most abundant molecular species, H_2 and CO, the properties of the halo have not been observationally well constrained.

Despite the lack of fine-tuning to match the characteristics of Perseus, the S11 model reproduces the observed $N(\text{HI})$, $N(\text{H}_2)$, and I_{CO} properties reasonably well. In particular, the predicted range of $N(\text{H}_2)$ in the scaled S11 model is in excellent agreement with our data. These results suggest that the time-dependent chemistry model is generally consistent with the time-independent chemistry model for a low-mass, old molecular cloud such as Perseus. However, there are several interesting discrepancies and they likely result from the nature of turbulence in the S11 model. The strong compressions and rarefactions by turbulence could result in the wider range of $N(\text{HI})$ in the S11 model and unlike the modified W10 model, there is no minimum $N(\text{HI})$ beyond which the rest of hydrogen is fully converted into H_2 . In addition, density fluctuations in the S11 model allow the formation of dense clumps even at small A_V and potentially result in a large scatter of I_{CO} . Turbulent motions could mix and spread the CO distribution, likely contributing to the scatter of I_{CO} . Our future studies of other Galactic molecular clouds, in particular those clouds much less evolved and/or forming more massive stars (therefore more turbulent) than Perseus, will be important for comprehensive tests of the PDR and MHD models.

We sincerely thank the anonymous referee for suggestions that significantly improved this work. We also thank Chris Carilli, Paul Clark, Jay Gallagher, Miller Goss, Paul Goldsmith, Harvey Liszt, Adam Leroy, Jürgen Ott, Josh Peek, and Jaime Pineda for stimulating discussions, Tom Dame for graciously providing his Dame et al. (2001) data, and the GALFA-HI and COMPLETE survey teams for making their data publicly available. M.-Y.L. and S.S. acknowledge support from the NSF grant AST-1056780, NASA through contract 145727 issued by JPL/Caltech, and the University of Wisconsin Graduate School. R.S., S.G., F.M., and R.K. acknowledge support from the Deutsche Forschungsgemeinschaft (DFG) via the SFB 881 (B1 and B2) “The Milky Way System” and the SPP (priority program) 1573. The Arecibo Observatory is operated by SRI

International under a cooperative agreement with the National Science Foundation (AST-1100968), and in alliance with Ana G. Méndez-Universidad Metropolitana, and the Universities Space Research Association. We have made use of the KARMA visualization software (Gooch 1996) and NASA’s Astrophysics Data System (ADS).

REFERENCES

- Abdo, A. A., Ackermann, M., Ajello, M., et al. 2010, *ApJ*, 710, 133
- Akritas, M. G. & Bershadsky, M. A. 1996, *ApJ*, 470, 706
- Ballesteros-Peredes, J., Vázquez-Semadeni, E., & Scalo, J. 1999, *ApJ*, 515, 286
- Ballesteros-Peredes, J., & Mac Low, M.-M. 2002, *ApJ*, 570, 734
- Bally, J., Walawender, J., Johnstone, D., Kirk, H., & Goodman, A. A. 2008, *Handbook of Star Forming Regions, Volume I: The Northern Sky*, ed. B. Reipurth (ASP Monograph Publications, Vol. 4; San Francisco, CA: ASP), 308
- Beaumont, C. N., Offner, S. S. R., Shetty, R., Glover, S. C. O., & Goodman, A. A. 2013, *ApJ*, 777, 173
- Bell, T. A., Roueff, E., Viti, S., & Williams, D. A. 2006, *MNRAS*, 371, 1865
- Bensch, F. 2006, *A&A*, 448, 1043
- Bevington, P. R. & Robinson, D. K. 2003, *Data Reduction and Error Analysis for the Physical Sciences*, 3rd ed. (Boston: McGraw-Hill)
- Bigiel, F., Leroy, A. K., Walter, F., et al. 2008, *AJ*, 136, 2846
- Bohlin, R. C., Savage, B. D., & Drake, J. F. 1978, *ApJ*, 224, 132
- Bolatto, A. D., Wolfire, M. G., & Leroy, A. K. 2013, *ARA&A*, 51, 207
- Boulanger, F., Abergel, A., Bernard, J.-P., et al. 1996, *A&A*, 312, 256
- Cardelli, J. A., Clayton, G. C., & Mathis, J. S. 1989, *ApJ*, 345, 245
- Černis, K. 1990, *Ap&SS*, 166, 315
- Cormier, D., Madden, S. C., Lebouteiller, V., et al. 2014, arXiv:1401.0563
- Dalgarno, A. 2006, *Proc. Natl. Acad. Sci.*, 103, 12269
- Dame, T. M., Hartmann, D., & Thaddeus, P. 2001, *ApJ*, 547, 792
- Draine, B. T. 1978, *ApJS*, 36, 595
- de Vries, H. W., Thaddeus, P., & Heithausen, A. 1987, *ApJ*, 319, 723
- Feldmann, R., Gnedin, N. Y., & Kravtsov, A. V. 2012a, *ApJ*, 747, 124
- Feldmann, R., Gnedin, N. Y., & Kravtsov, A. V. 2012b, *ApJ*, 758, 127
- Frerking, M. A., Langer, W. D., & Wilson, R. W. 1982, *ApJ*, 262, 590
- Gratier, P., Braine, J., Rodriguez-Fernandez, N. J., et al. 2010, *A&A*, 512, 68
- Glover, S. C. O., & Mac Low, M.-M. 2007a, *ApJS*, 169, 239
- Glover, S. C. O., & Mac Low, M.-M. 2007b, *ApJ*, 659, 1317
- Glover, S. C. O., Federrath, C., Mac Low, M.-M., & Klessen, R. S. 2010, *MNRAS*, 404, 2
- Glover, S. C. O., & Mac Low, M.-M. 2011, *MNRAS*, 412, 337
- Glover, S. C. O., & Clark, P. C. 2012, *MNRAS*, 426, 377
- González Hernández, J., Iglesias-Groth, S., Rebolo, R. et al. 2009, *ApJ*, 706, 866
- Gooch, R. 1996, *Astronomical Data Analysis Software and Systems V (ASP Conf. Ser. 101)*, ed. G. H. Jacoby & J. Barnes (San Francisco, CA: ASP), 80
- Goodman, A. A., Pineda, J. E., & Schnee, S. L. 2009, *ApJ*, 692, 91
- Gratier, P., Braine, J., Rodriguez-Fernandez, N. J., et al. 2010, *A&A*, 512, 68
- Heithausen, A., Bensch, F., Stutzki, J., Falgarone, E., & Panis, J. F. 1998, *A&A*, 331L, 65

- Heiles, C., & Troland, T. 2003, *ApJ*, 586, 1067
- Herbig, G. H., & Jones, B. F. 1983, *AJ*, 88, 1040
- Herbig, G. H. 1998, *ApJ*, 497, 736
- Heyer, M. H., & Brunt, C. M. 2004, *ApJ*, 615, 45
- Hollenbach, D. J., Kaufman, M. J., Neufeld, D., Wolfire, M., & Goicoechea, J. R. 2012, *ApJ*, 754, 105
- Hollenbach, D. J., & Tielens, A. G. G. M. 1997, *ARA&A*, 35, 179
- Imara, N., & Blitz, L. 2011, *ApJ*, 732, 78
- Imara, N., Bigiel, F., & Blitz, L. 2011, *ApJ*, 732, 79
- Indriolo, N., & McCall, B. J. 2012, *ApJ*, 745, 91
- Israel, F. P. 1997, *A&A*, 328, 471
- Kainulainen, J., Beuther, H., Henning, T., & Plume, R. 2009, *A&A*, 508, 35
- Kalberla, P. M. W., Burton, W. B., Hartmann, D., et al. 2005, *A&A*, 440, 775
- Kramer, C., Alves, J., Lada, C. et al. 1998, *A&A*, 329L, 33
- Knapp, G. R. 1974, *AJ*, 79, 527
- Kaufman, M. J., Wolfire, M. G., Hollenbach, D. J., & Luhman, M. L. 1999, *ApJ*, 527, 795
- Kaufman, M. J., Wolfire, M. G., & Hollenbach, D. J. 2006, *ApJ*, 644, 283
- Kennicutt, R. C. 1989, *ApJ*, 344, 685
- Kennicutt, R. C., & Evans, N. J. 2012, *ARA&A*, 50, 531
- Krumholz, M. R., McKee, C. F., & Tumlinson, J. 2009, *ApJ*, 693, 216 (K09)
- Krumholz, M. R., & Gnedin, N. Y. 2011, *ApJ*, 729, 36
- Krumholz, M. R. 2012, *ApJ*, 759, 9
- Lada, C. J., Lombardi, M., & Alves, J. F. 2010, *ApJ*, 724, 687
- Lagos, C., Bayet, E., Baugh, C. M., et al. 2012, *MNRAS*, 426, 2142
- Lazarian, A., Pogosyan, D., Vázquez-Semadeni, E., & Pichardo, B. 2001, *ApJ*, 555, 130
- Lee, M.-Y., Stanimirović, S., Douglas, K. A., et al. 2012, *ApJ*, 748, 75
- Lequeux, J. 2005, *The Interstellar Medium* (Berlin: Springer)
- Le Bourlot, J., Pineau Des Forets, G., Roueff, E., & Flower, D. R. 1993, *A&A*, 267, 233
- Le Petit, F., Nehmé, C., Le Bourlot, J., & Roueff, E. 2006, *ApJS*, 164, 506
- Leroy, A. K., Bolatto, A., Stanimirović, S., et al. 2007, *ApJ*, 658, 1027
- Leroy, A. K., Bolatto, A., Bot, C., et al. 2009, *ApJ*, 702, 352
- Leroy, A. K., Bolatto, A., Gordon, K., et al. 2011, *ApJ*, 737, 12
- Lombardi, M., Alves, J., & Lada, C. J. 2006, *A&A*, 454, 781
- Luhman, K. L., Rieke, G. H., Lada, C. J., & Lada, E. A. 1998, *ApJ*, 508, 347
- Mac Low, M.-M. & Klessen, R. 2004, *RvMP*, 76, 125
- Maloney, P., & Black, J. H. 1988, *ApJ*, 325, 389
- Mathis, J. S. 1990, *ARA&A*, 28, 37
- McKee, C. F., & Ostriker, E. C. 2007, *ARA&A*, 45, 565
- Magnani, L., Blitz, L., & Wouterloot, J. G. A. 1988, *ApJ*, 326, 909
- Miville-Deschênes, M.-A. & Lagache, G. 2005, *ApJS*, 157, 302
- Muench, A. A., Lada, E. A., Lada, C. J., et al. 2003, *AJ*, 125, 2029
- Narayanan, D., Krumholz, M. R., Ostriker, E. C., & Hernquist, L. 2012, *MNRAS*, 421, 3127
- Nelson, R. P., & Langer, W. D. 1999, *ApJ*, 524, 923
- Norman, M. L. 2000, *Rev. Mex. AA Ser. Conf.*, 9, 66
- Ossenkopf, V. 1997, *New Astron.*, 2, 365
- Ostriker, E. C., Stone, J., & Gammie, C. F. 2001, *ApJ*, 546, 980
- Papadopoulos, P. P., Thi, W.-F., & Viti, S. 2002, *ApJ*, 579, 270

- Paradis, D., Dobashi, K., Shimoikura, T., et al. 2012, *A&A*, 543, 103
- Peek, J. E. G., Heiles, C., Douglas, K. A., et al. 2011, *ApJS*, 194, 20
- Pineda, J. E., Caselli, P., & Goodman, A. A. 2008, *ApJ*, 679, 481
- Pineda, J. L., Goldsmith, P. F., Chapman, N., et al. 2010, *ApJ*, 721, 686
- Rahman, N., Bolatto, A. D., Xue, R., et al. 2012, 745, 183
- Reach, W. T., Koo, B.-C., & Heiles, C. 1994, *ApJ*, 429, 672
- Ridge, N. A., Di Francesco, J., Kirk, H., et al. 2006, *AJ*, 131, 2921
- Rogers, C., Heyer, M. H., & Dewdney, P. E. 1995, *ApJ*, 442, 694
- Sakamoto, S. 1996, *ApJ*, 462, 215
- Rubio, M., Lequeux, J., & Boulanger, F. 1993, *A&A*, 271, 9
- Sakamoto, S. 1999, *ApJ*, 523, 701
- Sancisi, R. Goss, W. M., Anderson, C., Johansson, L. E. B., & Winnberg, A. 1974, *A&A*, 35, 445
- Sandstrom, K. M., Leroy, A. K., Walter, F., et al. 2013, *ApJ*, 777, 5
- Schmidt, M. 1959, *ApJ*, 129, 243
- Schlegel, D. J., Finkbeiner, D. P., & Davis, M. 1998, *ApJ*, 500, 525
- Schruba, A., Leroy, A. K., Walter, F., et al. 2011, *AJ*, 142, 37
- Shetty, R., Glover, S. C., Dullemond, C. P., & Klessen, R. S. 2011a, *MNRAS*, 412, 1686 (S11)
- Shetty, R., Glover, S. C., Dullemond, C. P., et al. 2011b, *MNRAS*, 415, 3253
- Shetty, R., Kelly, B. C., & Bigiel, F. 2013, *MNRAS*, 430, 288
- Smith, P. A., Brand, P. W. J. L., Mountain, C. M., Puxley, P. J., & Nakai, N. 1991, *MNRAS*, 252, 6
- Sobolev, V. V. 1957, *SvA*, 1, 678
- Stone, J. M., & Norman, M. L. 1992, *ApJS*, 80, 753
- Taylor, S. D., Hartquist, T. W., & Williams, D. A. 1993, *MNRAS*, 264, 929
- Tielens, A. G. G. M., & Hollenbach, D. 1985, *ApJ*, 291, 722
- Wannier, P. G., Lichten, S. M., & Morris, M. 1983, *ApJ*, 268, 727
- Wannier, P. G., Lichten, S. M., Andersson, B.-G., & Morris, M. 1991, *ApJS*, 75, 978
- Williams, J. P., & Maddalena, R. J. 1996, *ApJ*, 464, 247
- Wolfire, M. G., Hollenbach, D., & Tielens, A. G. G. M. 1993, *ApJ*, 402, 195
- Wolfire, M. G., McKee, C. F., Hollenbach, D., & Tielens, A. G. G. M. 2003, *ApJ*, 587, 278
- Wolfire, M. G., Tielens, A. G. G. M., Hollenbach, D., & Kaufman, M. J. 2008, *ApJ*, 680, 384
- Wolfire, M. G., Hollenbach, D., & McKee, C. 2010, *ApJ*, 716, 1191 (W10)
- Young, J. S., Goldsmith, P. F., Langer, W. D., Wilson, R. W., & Carlson, E. R. 1982, 261, 513

TABLE 1
PHYSICAL PROPERTIES OF THE DARK AND STAR-FORMING REGIONS

Region	α^a (J2000)	δ^a (J2000)	Average Size ^b (pc)	$\Sigma N(\text{H}_2)/\Sigma I_{\text{CO}}$ ($\text{cm}^{-2} \text{K}^{-1} \text{km}^{-1} \text{s}$)	Median σ_{CO} (km s^{-1})
B5	3.71 ^h – 3.84 ^h	32.57° – 33.29°	5	5.0×10^{19}	1.3
IC348	3.69 ^h – 3.81 ^h	31.14° – 32.50°	6	6.6×10^{19}	1.4
B1E/B1	3.52 ^h – 3.65 ^h	30.57° – 32.14°	6	2.7×10^{19}	1.8
NGC1333	3.44 ^h – 3.52 ^h	30.50° – 32.21°	7	1.9×10^{19}	2.0
L1448	3.36 ^h – 3.44 ^h	30.21° – 31.14°	5	1.5×10^{19}	1.3

^a The regional boundaries defined in Section 4.

^b The characteristic size of each region calculated by $(\text{total number of pixels})^{1/2} \times 0.38 \text{ pc}$, where 0.38 pc is the physical size of one pixel.

TABLE 2
PREDICTIONS FROM THE MODIFIED W10 MODEL WITH A “CORE-HALO” DENSITY DISTRIBUTION^a

	$n_{\text{core}} = 10^3 \text{ cm}^{-3}$	$n_{\text{core}} = 5 \times 10^3 \text{ cm}^{-3}$	$n_{\text{core}} = 10^4 \text{ cm}^{-3}$
$N(\text{HI})^b$ (cm^{-2})	$9.00 \times 10^{20} - 9.60 \times 10^{20}$	$8.98 \times 10^{20} - 9.20 \times 10^{20}$	$8.96 \times 10^{20} - 9.04 \times 10^{20}$
$N(\text{H}_2)^b$ (cm^{-2})	$1.75 \times 10^{20} - 4.52 \times 10^{21}$	$1.75 \times 10^{20} - 4.54 \times 10^{21}$	$1.75 \times 10^{20} - 4.55 \times 10^{21}$
$R_{\text{H}_2}^b$	0.39 – 9.42	0.39 – 9.87	0.39 – 10.11
I_{CO}^b (K km s^{-1})	0.075 – 36.90	0.33 – 41.40	0.39 – 33.90
L_{halo}^c (pc)	7.28	7.28	7.28
$L_{\text{core}}^{b,d}$ (pc)	0.11 – 2.94	0.023 – 0.59	0.011 – 0.29
$L_{\text{halo-core}}^{b,e}$ (pc)	7.39 – 10.22	7.30 – 7.87	7.29 – 7.57
$\langle n \rangle^{b,f}$ (cm^{-3})	54.74 – 316.66	55.42 – 411.21	55.49 – 427.51

^a For all three models, $n_{\text{halo}} = 40 \text{ cm}^{-3}$.

^b The values are provided for the minimum and maximum column densities ($A_V = 1.25 \text{ mag}$ and 10 mag).

^c The size of the diffuse halo $L_{\text{halo}} = 9 \times 10^{20} \text{ cm}^{-2}/40 \text{ cm}^{-3}$.

^d The size of the dense core $L_{\text{core}} = (N(\text{H}) - 9 \times 10^{20})/n_{\text{core}}$.

^e The total size of the slab $L_{\text{halo-core}} = L_{\text{halo}} + L_{\text{core}}$.

^f The average density $\langle n \rangle = N(\text{H})/L_{\text{halo-core}}$.

TABLE 3
PREDICTIONS FROM THE MODIFIED W10 MODEL WITH A UNIFORM DENSITY DISTRIBUTION

	$n = 10^3 \text{ cm}^{-3}$	$n = 5 \times 10^3 \text{ cm}^{-3}$	$n = 10^4 \text{ cm}^{-3}$
$N(\text{HI})^a$ (cm^{-2})	$5.71 \times 10^{19} - 1.30 \times 10^{20}$	$1.15 \times 10^{19} - 2.66 \times 10^{19}$	$5.59 \times 10^{18} - 1.33 \times 10^{19}$
$N(\text{H}_2)^a$ (cm^{-2})	$2.72 \times 10^{20} - 4.94 \times 10^{21}$	$2.95 \times 10^{20} - 4.99 \times 10^{21}$	$2.98 \times 10^{20} - 5.00 \times 10^{21}$
$R_{\text{H}_2}^a$	9.53 – 76.00	51.30 – 375.19	106.62 – 751.88
I_{CO}^a (K km s^{-1})	0.84 – 46.90	9.79 – 62.40	18.00 – 60.20
$L_{\text{uniform}}^{a,b}$ (pc)	0.19 – 3.24	0.039 – 0.65	0.019 – 0.32

^a The values are provided for the minimum and maximum column densities ($A_V = 0.6 \text{ mag}$ and 10 mag).

^b The total size of the slab $L_{\text{uniform}} = N(\text{H})/n$.

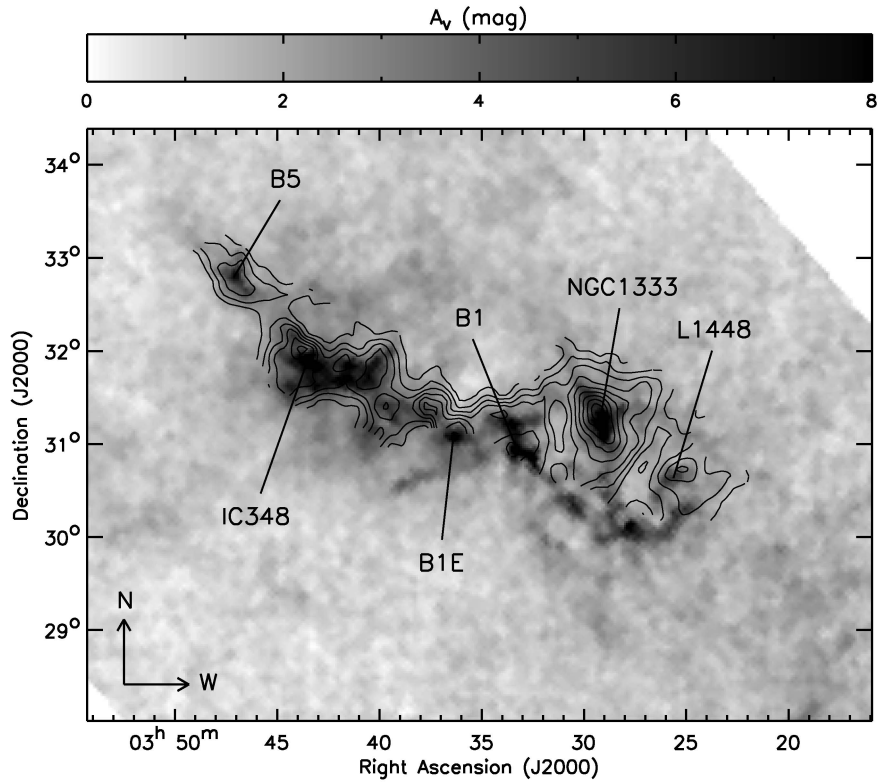


Fig. 1.— COMPLETE A_V image of Perseus overlaid with the COMPLETE I_{CO} contours (Ridge et al. 2006). The contour levels range from 10% to 90% of the peak (80 K km s^{-1}) with 10% steps. The angular resolution of the A_V and I_{CO} images here is $5'$ and $4.3'$ respectively. A number of dark (B5, B1E, B1, and L1448) and star-forming regions (IC348 and NGC1333) are labelled.

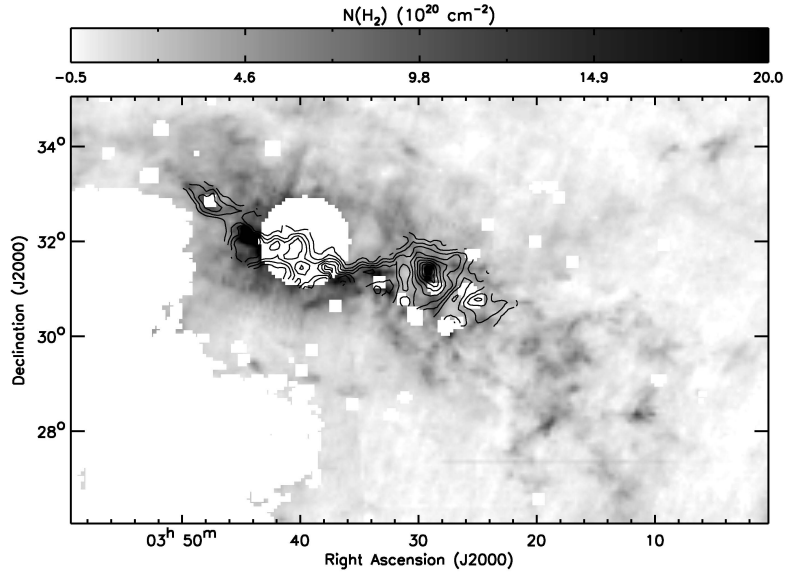


Fig. 2.— $N(\text{H}_2)$ image at $4.3'$ angular resolution derived by Lee et al. (2012). The COMPLETE I_{CO} contours are overlaid in black and their levels range from 10% to 90% of the peak (80 K km s^{-1}) with 10% steps. The blank data points correspond to point sources and regions with possible contamination (the Taurus molecular cloud and a background HII region). See Sections 4.2 and 4.3 of Lee et al. (2012) for details.

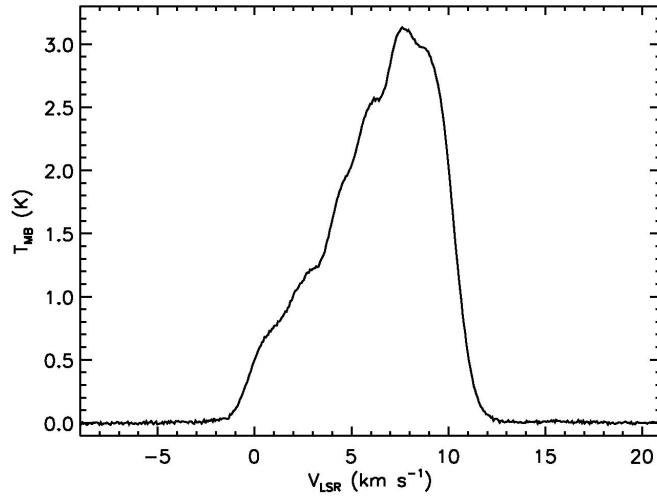


Fig. 3.— CO spectrum obtained by averaging the COMPLETE CO spectra of all data points where the ratio of the peak main-beam brightness temperature to the rms noise is greater than 3. Note that the CO emission shows multiple velocity components.

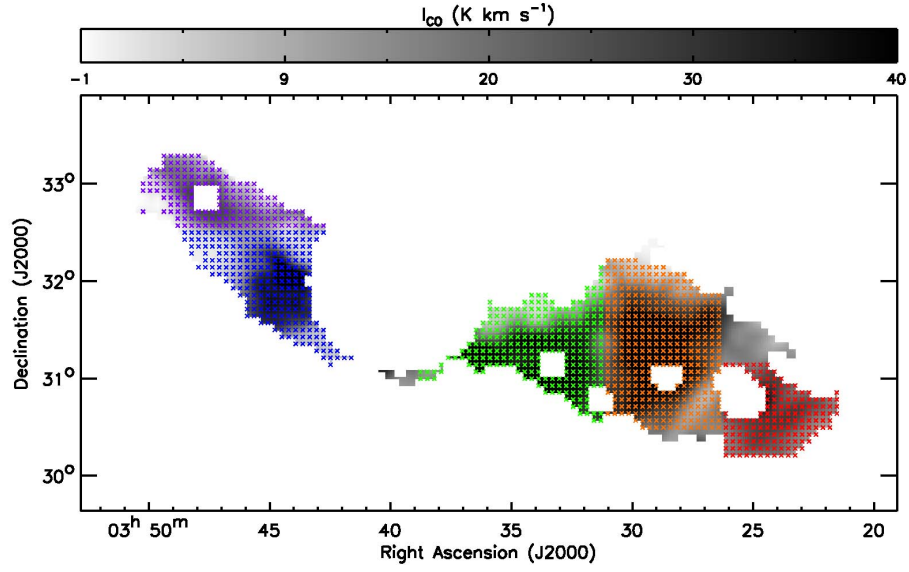


Fig. 4.— Each of the five regions is overlaid on the COMPLETE I_{CO} image in different color. B5 is purple, IC348 is blue, B1E/B1 is green, NGC1333 is orange, and L1448 is red. See Section 4 for details on how we determined these regions.

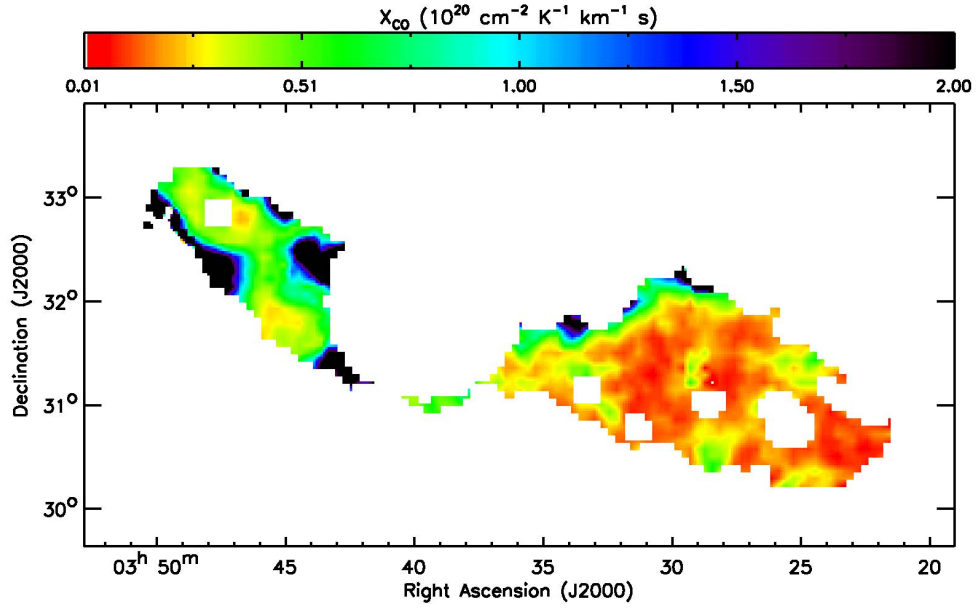


Fig. 5.— X_{CO} image at $4.3'$ angular resolution.

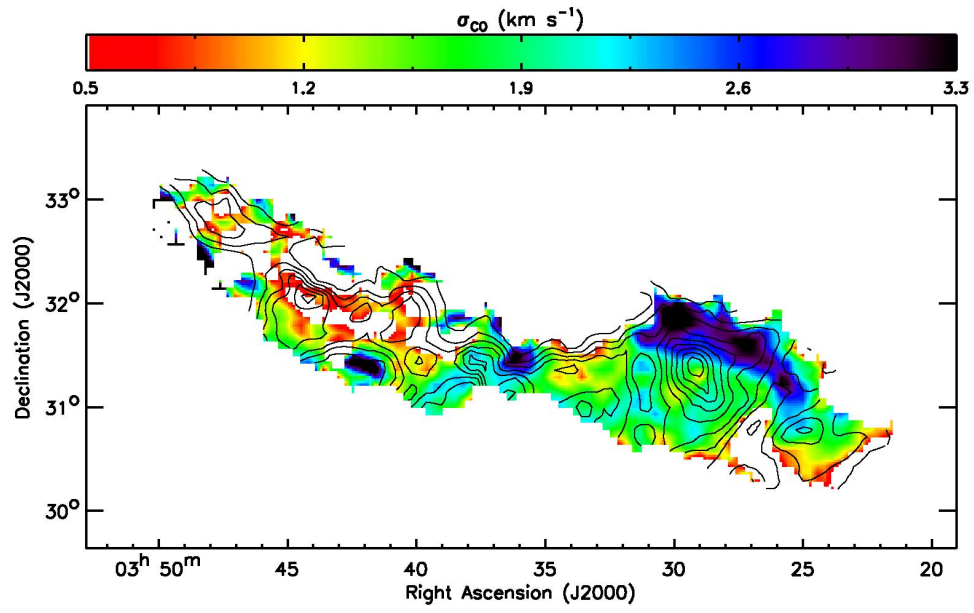


Fig. 6.— σ_{CO} image overlaid with the COMPLETE I_{CO} contours. The contour levels range from 10% to 90% of the peak (80 K km s^{-1}) with 10% steps.

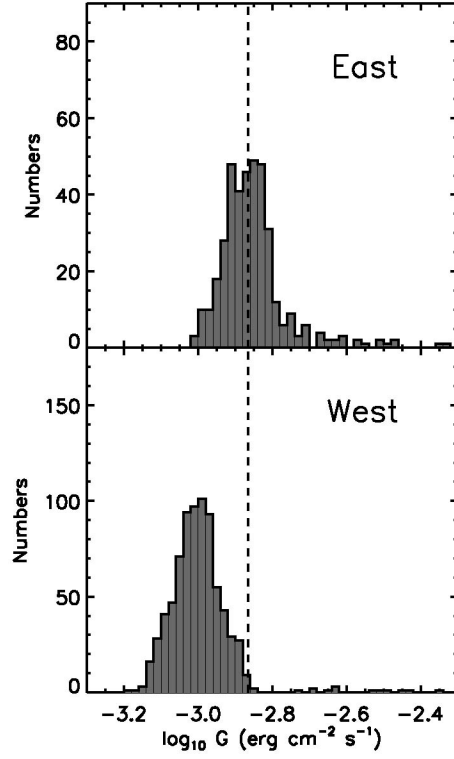


Fig. 7.— Histograms of G . B5/IC348 and B1E/B1/NGC1333/L1448 are combined to produce the histograms of *East* and *West*. The median G of *East* ($\sim 10^{-2.86}$ erg cm $^{-2}$ s $^{-1}$) is shown as a dashed line.

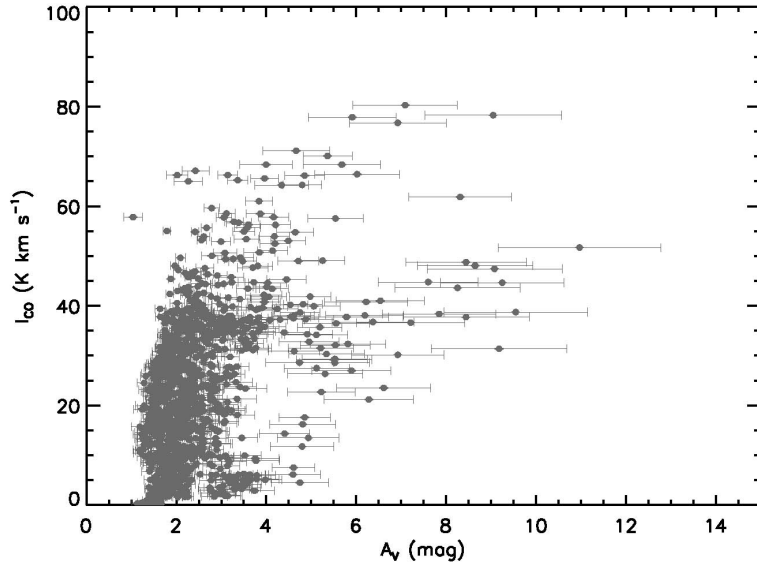


Fig. 8.— COMPLETE I_{CO} as a function of A_V for all five regions defined in Section 4.

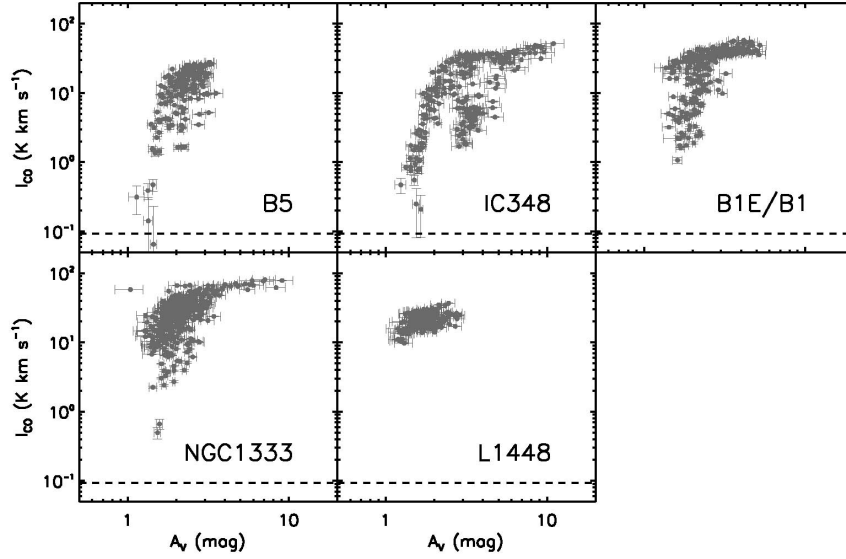


Fig. 9.— COMPLETE I_{CO} as a function of A_V for each dark and star-forming region. The mean 1σ uncertainty of I_{CO} ($\sim 0.09 \text{ K km s}^{-1}$) is shown as a dashed line, while that of A_V ($\sim 0.2 \text{ mag}$) is too small to be shown.

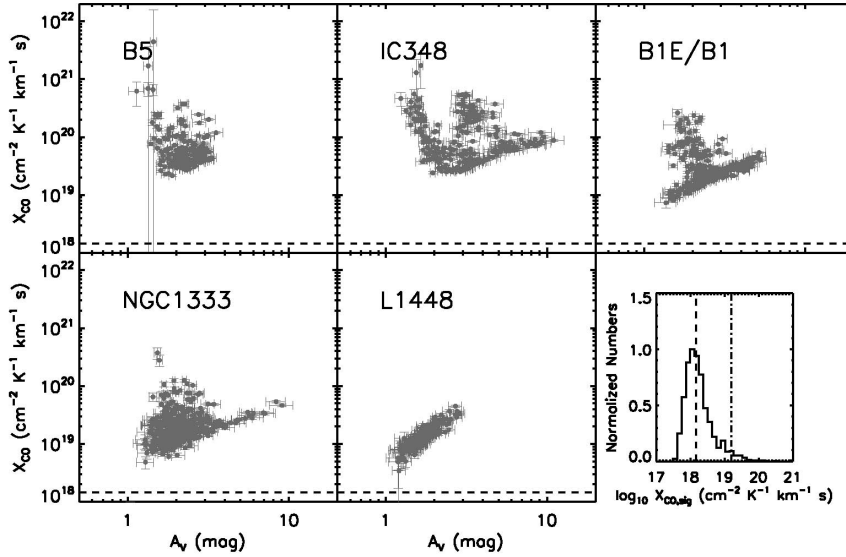


Fig. 10.— X_{CO} as a function of A_V for each dark and star-forming region. The median 1σ uncertainty of X_{CO} ($\sim 1.5 \times 10^{18}$) is shown as a dashed line, while the mean 1σ uncertainty of A_V ($\sim 0.2 \text{ mag}$) is too small to be shown. Note that we show the median 1σ instead of the mean 1σ , because it is a better representative of the uncertainty in X_{CO} . The right lowermost panel shows a normalized histogram of the 1σ uncertainty in X_{CO} and it is clear that the mean 1σ shown as a dashed-dot line corresponds to the high end of the distribution, affected by a small fraction of the data points with large uncertainties.

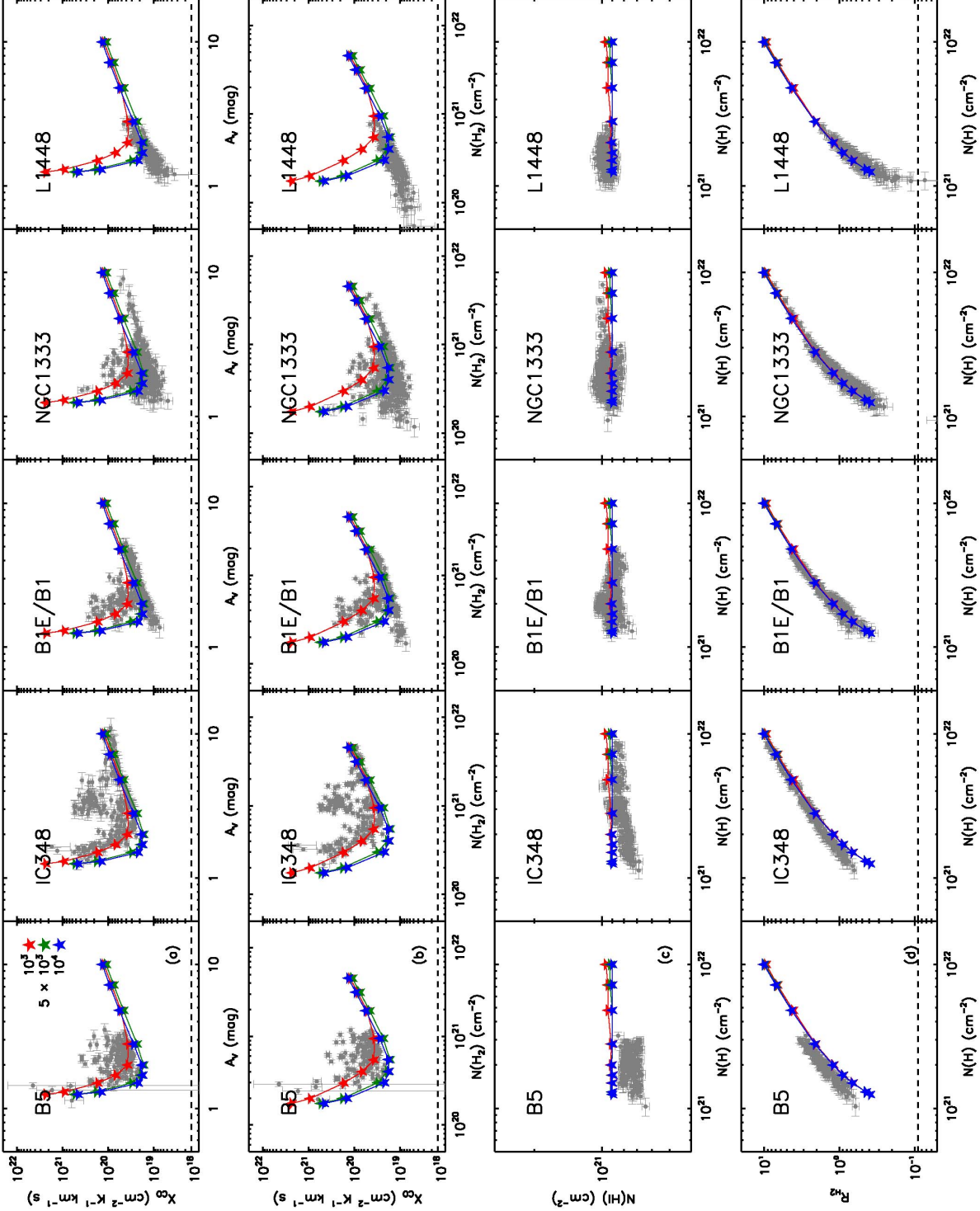


Fig. 11.— Comparison with the modified W10 model. Model predictions for $n_{\text{core}} = 10^3, 5 \times 10^3, \text{ and } 10^4 \text{ cm}^{-3}$ are shown as red, green, and blue stars respectively. The mean 1σ uncertainty of R_{H_2} (~ 0.09) is shown as a dashed line, while those of A_V ($\sim 0.2 \text{ mag}$), $N(\text{H}_2)$ ($\sim 3.3 \times 10^{19} \text{ cm}^{-2}$), $N(\text{HI})$ ($\sim 3.5 \times 10^{19} \text{ cm}^{-2}$), and $N(\text{H})$ ($\sim 1.6 \times 10^{20} \text{ cm}^{-2}$) are too small to be shown. The median 1σ uncertainty of X_{CO} ($\sim 1.5 \times 10^{18}$) is shown as a dashed line as well. (a) X_{CO} vs A_V . (b) X_{CO} vs $N(\text{H}_2)$. (c) $N(\text{HI})$ vs $N(\text{H})$. (d) R_{H_2} vs $N(\text{H})$.

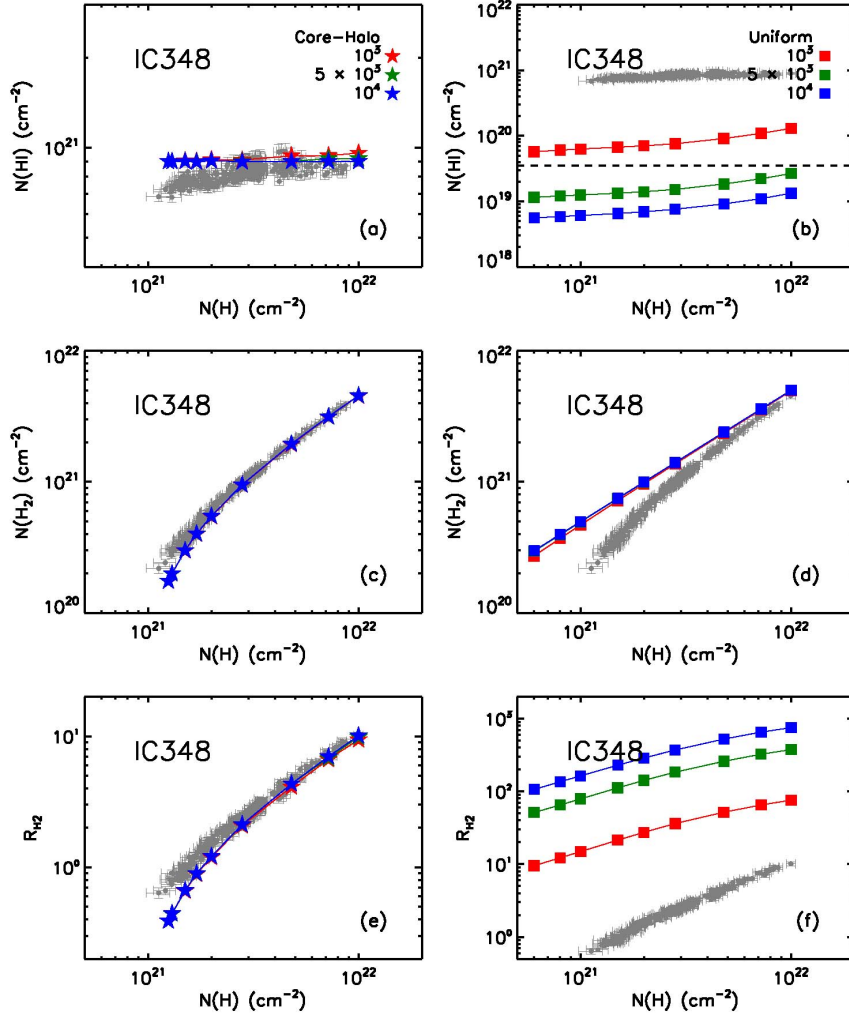


Fig. 12.— Comparison with the modified W10 model for IC348. The mean 1σ uncertainties of $N(\text{HI})$ ($\sim 3.5 \times 10^{19} \text{ cm}^{-2}$) and I_{CO} ($\sim 0.09 \text{ K km s}^{-1}$) are shown as dashed lines, while those of $N(\text{H})$ ($\sim 1.6 \times 10^{20} \text{ cm}^{-2}$), $N(\text{H}_2)$ ($\sim 3.3 \times 10^{19} \text{ cm}^{-2}$), R_{H_2} (~ 0.09), and A_V ($\sim 0.2 \text{ mag}$) are too small to be shown. The median 1σ uncertainty of X_{CO} ($\sim 1.5 \times 10^{18}$) is shown as a dashed line as well. (Left) The modified W10 model with the “core-halo” structure is shown with red, green, and blue stars ($n_{\text{core}} = 10^3$, 5×10^3 , and 10^4 cm^{-3}). (Right) The modified W10 model with the uniform density distribution is shown with red, green, and blue squares ($n = 10^3$, 5×10^3 , and 10^4 cm^{-3}).

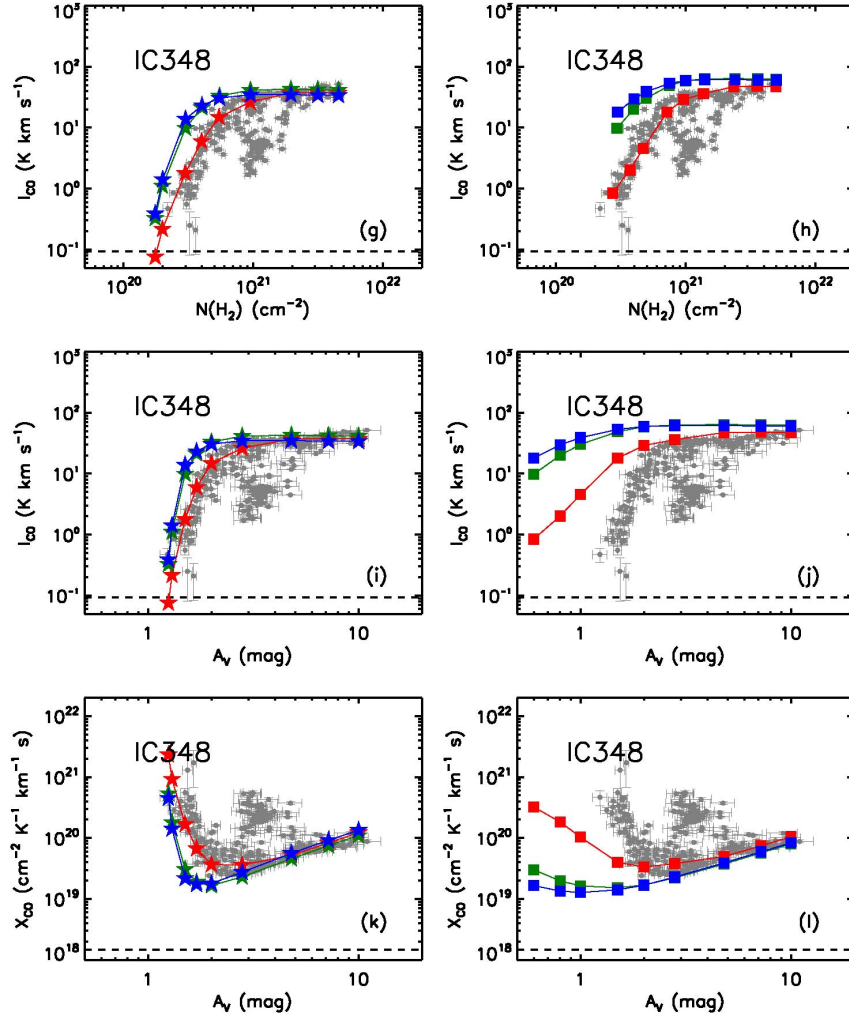


Fig. 12.— (Continued)

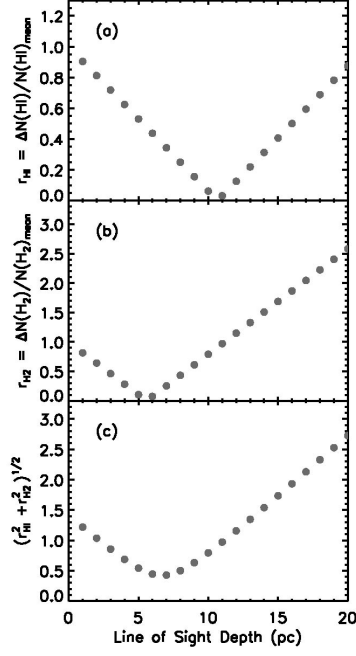


Fig. 13.— (a) The difference between the observed mean $N(\text{HI})$ and the simulated mean $N(\text{HI})$ normalized by the observed mean $N(\text{HI})$, $r_{\text{HI}} = \Delta N(\text{HI})/N(\text{HI})_{\text{mean}}$, is plotted as a function of line of sight depth. (b) Same as (a) but for $N(\text{H}_2)$. (c) The sum of the two normalized differences in quadrature, $\sqrt{r_{\text{HI}}^2 + r_{\text{H}_2}^2}$, is plotted as a function of line of sight depth. Note that the line of sight depth of 7 pc results in the minimum discrepancy between our and simulated data.

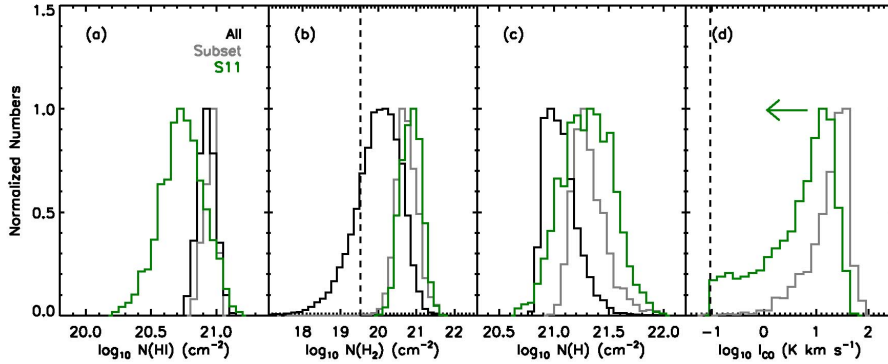


Fig. 14.— Normalized histograms of $N(\text{HI})$, $N(\text{H}_2)$, $N(\text{H})$, and I_{CO} . The histograms in black, grey, and green are constructed using the data points with positive $N(\text{H}_2)$, shown in Figure 4, and from the S11 model respectively. For the S11 model, the simulated $N(\text{HI})$, $N(\text{H}_2)$, and $N(\text{H})$ data are scaled for 7 pc, while the simulated I_{CO} data are not. See Section 7.2.2 for details. The mean 1σ uncertainties of $N(\text{H}_2)$ ($\sim 3.3 \times 10^{19} \text{ cm}^{-2}$) and I_{CO} ($\sim 0.09 \text{ K km s}^{-1}$) are shown as dashed lines, while those of $N(\text{HI})$ ($\sim 3.5 \times 10^{19} \text{ cm}^{-2}$) and $N(\text{H})$ ($\sim 1.6 \times 10^{20} \text{ cm}^{-2}$) are too small to be shown.

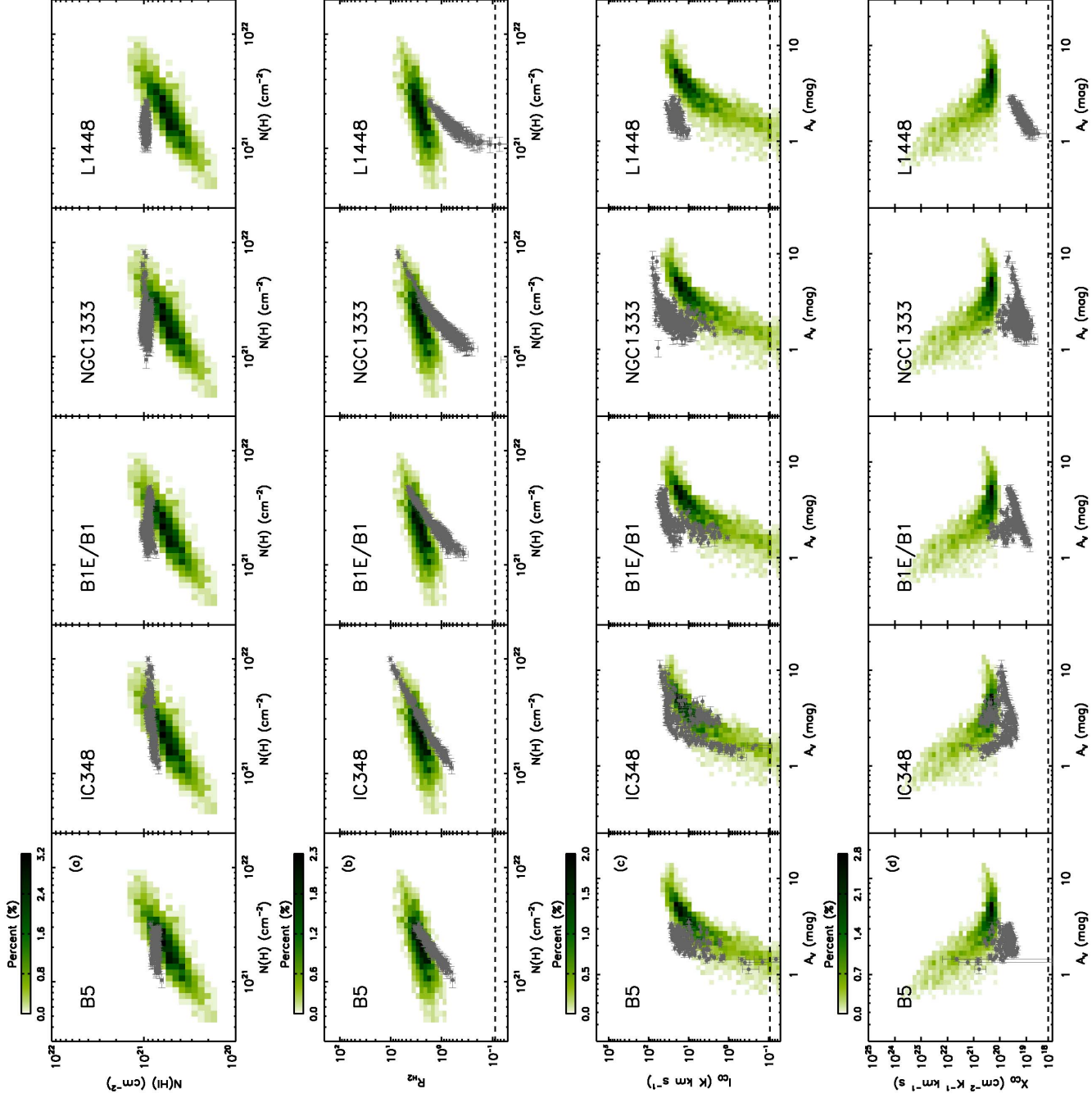


Fig. 15. — Comparison with the S11 model. The mean 1σ uncertainties of R_{H_2} (~ 0.09) and I_{CO} ($\sim 0.09 \text{ K km s}^{-1}$) are shown as dashed lines, while those of $N(\text{HI})$ ($\sim 3.5 \times 10^{19} \text{ cm}^{-2}$), $N(\text{H})$ ($\sim 1.6 \times 10^{20} \text{ cm}^{-2}$) and A_V ($\sim 0.2 \text{ mag}$) are too small to be shown. The median 1σ uncertainty of X_{CO} ($\sim 1.5 \times 10^{18}$) is shown as a dashed line as well. (a) $N(\text{HI})$ vs $N(\text{H})$. (b) R_{H_2} vs $N(\text{H})$. (c) I_{CO} vs A_V . (d) X_{CO} vs A_V . For (a) and (b), the simulated quantities are smoothed, regridded, and scaled for 7 pc. In addition, the thresholds for $N(\text{H}_2)$ and I_{CO} are applied. On the other hand, for (c) and (d), the simulated quantities are smoothed and regridded but neither the scaling nor the thresholds is applied. See Section 7.2.3 for details.

A. Detailed Comparison With Previous Studies

While we found $\langle X_{\text{CO}} \rangle \sim 3 \times 10^{19}$ for Perseus, Dame et al. (2001) and Pineda et al. (2008) estimated $\sim 1.2 \times 10^{20}$ and $\sim 1.4 \times 10^{20}$ respectively. These two studies are similar with our study in the sense that they utilized dust as a tracer of total gas column density, but applied different methodologies to derive X_{CO} . We follow their methodologies in order to understand why our result is different.

A.1. Comparison with Dame et al. (2001)

Dame et al. (2001) used the $E(B - V)$ data from Schlegel et al. (1998) and the HI data from the LAB survey. They estimated DGR on large-scales by smoothing both the $E(B - V)$ and $N(\text{HI})$ images to $10''$ resolution and calculating the ratio of the smoothed $E(B - V)$ and $N(\text{HI})$ images. The $E(B - V)$ image was then divided by the large-scale DGR image and $N(\text{HI})$ was subtracted to derive $N(\text{H}_2)$. The derived $N(\text{H}_2)$ was finally combined with I_{CO} from the CfA survey to estimate X_{CO} . The resolution of the HI data was the lowest among all data sets and the estimated X_{CO} values were consequently at $36''$ resolution. We note that most other large-scale studies of X_{CO} in the Milky Way are also at $36''$ resolution, limited by the LAB HI data (e.g., Abdo et al. 2010; Paradis et al. 2012).

To show how different resolutions and methodologies affect the estimation of X_{CO} , we first compare our original data at $4.3''$ resolution (black histograms; data points for all five regions) with (1) our data smoothed to $36''$ resolution (grey histograms) and (2) the data from Dame et al. (2001) (green histograms) in Figure 16. Note that we use the CfA CO data here to derive X_{CO} at $36''$ resolution instead of the COMPLETE CO data we used elsewhere in this paper, because of their larger spatial coverage ($\sim 10^\circ \times 7^\circ$ for the CfA CO vs $\sim 6^\circ \times 3^\circ$ for the COMPLETE CO). This will not cause any complication with our comparison, considering that $\sim 83\%$ of the data points are consistent within 1σ uncertainties when the CfA and COMPLETE CO data are compared at the common resolution of $8.4''$. For each histogram in Figure 16, we show the mean value of the distribution as a dashed line. In the case of X_{CO} , $\langle X_{\text{CO}} \rangle$ calculated as $\Sigma N(\text{H}_2) / \Sigma I_{\text{CO}}$ is shown instead.

In comparison between our data at $4.3''$ and $36''$ resolutions, we find that $\langle X_{\text{CO}} \rangle$ increases from $\sim 3 \times 10^{19}$ ($4.3''$) to $\sim 4.5 \times 10^{19}$ ($36''$). $\langle X_{\text{CO}} \rangle$ increases because spatial smoothing affects the I_{CO} distribution slightly more than the $N(\text{H}_2)$ distribution. To be precise, I_{CO} decreases by a factor of ~ 6 from $\sim 23.1 \text{ K km s}^{-1}$ to $\sim 3.9 \text{ K km s}^{-1}$ on average, while $N(\text{H}_2)$ decreases by a factor of ~ 4 from $\sim 6.9 \times 10^{20} \text{ cm}^{-2}$ to $\sim 1.7 \times 10^{20} \text{ cm}^{-2}$ on average.

While spatial smoothing to $36''$ resolution results in the slight increase of X_{CO} , there is still a factor of ~ 2.7 discrepancy between our $\langle X_{\text{CO}} \rangle \sim 4.5 \times 10^{19}$ and the value derived by Dame et al. (2001) for the same area. Because the same CfA CO data were used, as shown from the good agreement between the grey and green histograms in Figure 16(c), the discrepancy in X_{CO} would come from the difference in $N(\text{H}_2)$ and we indeed find that the mean $N(\text{H}_2) \sim 5.2 \times 10^{20} \text{ cm}^{-2}$ in Dame et al. (2001) is larger than our mean $N(\text{H}_2) \sim 1.7 \times 10^{20} \text{ cm}^{-2}$ at $36''$ resolution by a factor of ~ 3 . Considering that the equations for deriving $N(\text{H}_2)$ in our study and Dame et al. (2001) are essentially the same, $N(\text{H}_2) = (A_V / \text{DGR} - N(\text{HI})) \times 0.5$, we compare our A_V and $N(\text{HI})$ data smoothed to $36''$ resolution with the data from Dame et al. (2001) in Figures 16(d,f). To convert $E(B - V)$ in Dame et al. (2001) into A_V , we use the total-to-selective extinction ratio $R_V \sim 3.1$ for the diffuse ISM (Mathis 1990). In addition, the local DGR $\sim 1.1 \times 10^{-21} \text{ mag cm}^{-2}$ Lee et al. (2012) derived for Perseus is compared with the DGR data from Dame et al. (2001) in Figure

16(e). While we find that our A_V at $36'$ resolution is consistent with A_V in Dame et al. (2001), our $N(\text{HI})$ is slightly smaller than theirs by a factor of ~ 1.4 on average. This difference mainly results from the fact that Dame et al. (2001) integrated the HI emission along a whole line of sight, while our $N(\text{HI})$ was derived by integrating the HI emission over the velocity range for Perseus, from -5 km s^{-1} to $+15 \text{ km s}^{-1}$ (Section 3.1). The slightly smaller $N(\text{HI})$ in our study could affect the estimation of DGR and we indeed find that the local DGR for Perseus is larger than the mean DGR in Dame et al. (2001) by a factor of ~ 1.7 on average. Another factor that could affect DGR is spatial smoothing to 10° resolution done by Dame et al. (2001). Specifically, they blanked all pixels whose I_{CO} is larger than 1 K km s^{-1} and replaced the blanked pixels with the Gaussian-weighted $E(B - V)/N(\text{HI})$ values, the Gaussian having a FWHM of 10° . The angular size of 10° is comparable to the size of Perseus and in this case spatial smoothing could result in the inclusion of the diffuse ISM with small DGR in the far outskirts of the cloud.

A.2. Comparison with Pineda et al. (2008)

Pineda et al. (2008) used the A_V and I_{CO} images from the COMPLETE survey smoothed to $5'$ resolution and derived X_{CO} for Perseus by fitting a linear function to I_{CO} vs A_V under the following two assumptions: (a1) all hydrogen traced by A_V is in the form of H_2 and (a2) $\text{DGR} = 5.3 \times 10^{-22} \text{ mag cm}^2$, the typical Galactic value (Bohlin et al. 1978). Considering that our study uses essentially the same data sets, the COMPLETE I_{CO} image and the A_V image calibrated with the COMPLETE A_V data, any difference in X_{CO} would come from different methodologies for deriving X_{CO} . In Figure 17(a), we plot I_{CO} as a function of A_V for Perseus and fit a linear function to the data as Pineda et al. (2008) did. To be consistent with Pineda et al. (2008), we smooth our I_{CO} and A_V images with Gaussian kernels to obtain a resolution of $5'$ and regrid the images to a grid of $2.5'$. In addition, we use their primary thresholds, i.e., the CO and ^{13}CO integrated intensities are positive and the CO and ^{13}CO peak brightness temperatures are at least 10 and 5 times the rms noises of CO and ^{13}CO , to select data points. We do not consider other thresholds adopted in Pineda et al. (2008), e.g., exclusion of the data points with a stellar density larger than 10 stars per pixel, and expect that they will not make a significant change in the linear fit, considering that they account only a small fraction of the total number of data points ($\sim 7\%$). As Pineda et al. (2008) performed, we fit the linear function

$$A_V = a + bI_{\text{CO}} \quad (\text{A1})$$

using the bivariate correlated errors and intrinsic scatter estimator (BCES; Akritas & Bershady 1996) and find $a = -0.22 \pm 0.13 \text{ mag}$ and $b = 0.10 \pm 0.01 \text{ mag K}^{-1} \text{ km}^{-1} \text{ s}$. This result is consistent with Pineda et al. (2008), once our fitted parameters a and b are converted into the quantities in Equation (18) of Pineda et al. (2008), $A_{V12} = a = -0.22 \pm 0.13 \text{ mag}$ and $X_2 = b \times 9.4 \times 10^{20} = (1.0 \pm 0.1) \times 10^{20}$, where A_{V12} is the minimum A_V below which there is no CO emission and X_2 is essentially X_{CO} . Our $X_2 = (1.0 \pm 0.1) \times 10^{20}$ is very close to $X_2 = (1.4 \pm 0.1) \times 10^{20}$ in Pineda et al. (2008). In summary, our result is consistent with Pineda et al. (2008) if we use exactly the same methodology for deriving $N(\text{H}_2)$ and X_{CO} .

However, instead of fitting a linear function to I_{CO} vs A_V , we derive X_{CO} on a pixel-by-pixel basis in this paper. To investigate whether this could result in a significant difference, we perform additional tests. First, we derive X_{CO} by assuming (a1) but with our $\text{DGR} = 1.1 \times 10^{-21} \text{ mag cm}^2$. The result is shown in Figure 17(b) (grey histogram), along with our original X_{CO} distribution (black histogram). Second, we assume both (a1) and (a2) and still derive X_{CO} on a pixel-by-pixel basis. The result is shown in the same panel as a green histogram. In addition, $\langle X_{\text{CO}} \rangle$ for each histogram is calculated as $\Sigma N(\text{H}_2)/\Sigma I_{\text{CO}}$ and is shown as a dashed line. We find $\langle X_{\text{CO}} \rangle \sim 4.9 \times 10^{19}$ and 1×10^{20} for the first and second test respectively.

This suggests that our pixel-by-pixel derivation of X_{CO} is consistent with the linear fit method in Pineda et al. (2008) and therefore the discrepancy between our $\langle X_{\text{CO}} \rangle$ and X_{CO} in Pineda et al. (2008) results from the assumptions (a1) and (a2). Specifically, the neglect of $N(\text{HI})$ in derivation of $N(\text{H}_2)$ (a1) results in a factor of ~ 1.6 difference in $\langle X_{\text{CO}} \rangle$, while the use of the Galactic DGR (a2) results in an additional factor of ~ 2 difference.

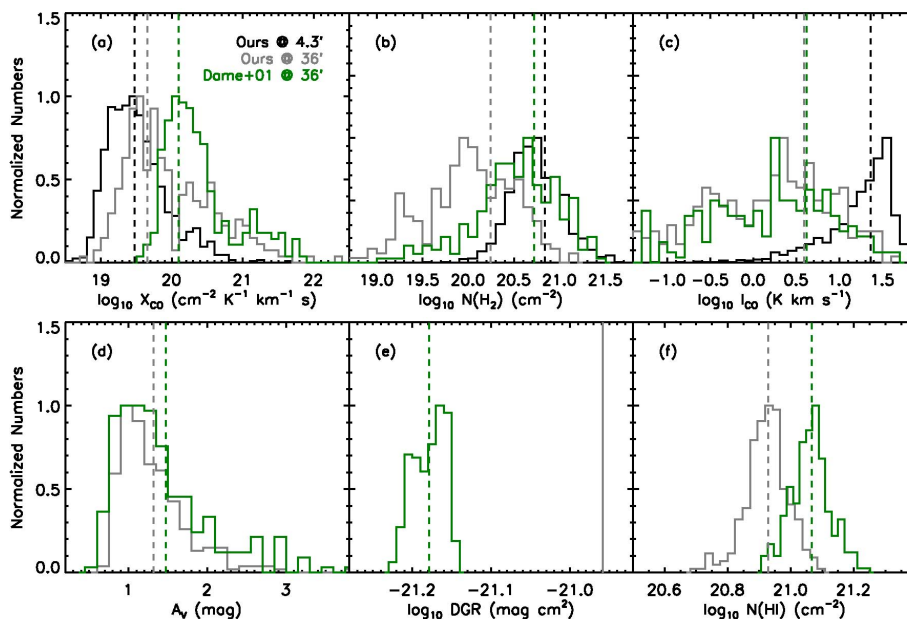


Fig. 16.— Comparison with Dame et al. (2001). The black and grey histograms represent the data from our study at 4.3' and 36' angular resolutions, while the green histograms show the data from Dame et al. (2001). All histograms are normalized for easy comparison. Note that the I_{CO} image from the CfA survey was combined with our $N(\text{H}_2)$ image to derive X_{CO} at 36' angular resolution. Dashed lines show the mean values of individual quantities, except for those shown in (a), which represent $\langle X_{\text{CO}} \rangle = \Sigma N(\text{H}_2) / \Sigma I_{\text{CO}}$. The local $\text{DGR} = 1.1 \times 10^{-21} \text{ mag cm}^2$ Lee et al. (2012) derived for Perseus is shown as a grey solid line.

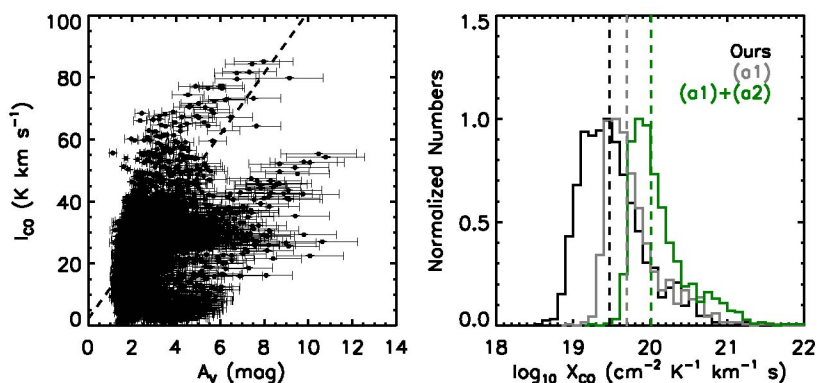


Fig. 17.— Comparison with Pineda et al. (2008). (Left) I_{CO} vs A_V . The linear fit obtained from the BCES is shown as a dashed line. (Right) Normalized histograms of X_{CO} . The black histogram is our original X_{CO} at 4.3' angular resolution, while the grey and green histograms show X_{CO} estimated by assuming (a1) only and (a1) + (a2) respectively. Dashed lines show $\langle X_{\text{CO}} \rangle = \Sigma N(\text{H}_2) / \Sigma I_{\text{CO}}$.